

# Sampling from multimodal distributions using tempered Hamiltonian transitions

Joonha Park

University of Kansas

## Abstract

Hamiltonian Monte Carlo (HMC) methods are widely used to draw samples from unnormalized target densities due to high efficiency and favorable scalability with respect to increasing space dimensions. However, HMC struggles when the target distribution is multimodal, because the maximum increase in the potential energy function (i.e., the negative log density function) along the simulated path is bounded by the initial kinetic energy, which follows a half of the  $\chi_d^2$  distribution, where  $d$  is the space dimension. In this paper, we develop a Hamiltonian Monte Carlo method where the constructed paths can travel across high potential energy barriers. This method does not require the modes of the target distribution to be known in advance. Our approach enables frequent jumps between the isolated modes of the target density by continuously varying the mass of the simulated particle while the Hamiltonian path is constructed. Thus, this method can be considered as a combination of HMC and the tempered transitions method. Compared to other tempering methods, our method has a distinctive advantage in the Gibbs sampler settings, where the target distribution changes at each step. We develop a practical tuning strategy for our method and demonstrate that it can construct globally mixing Markov chains targeting high-dimensional, multimodal distributions, using mixtures of normals and a sensor network localization problem.

**Keywords:** Hamiltonian Monte Carlo; Markov chain Monte Carlo; tempered transitions; multimodality

## 1 Introduction

Hamiltonian Monte Carlo (HMC) is a class of Markov chain Monte Carlo (MCMC) methods that use the Hamiltonian dynamics to draw sample points from an unnormalized target density (Duane et al., 1987). HMC enjoys more favorable scaling properties with increasing space dimensions than other commonly used MCMC algorithms, such as random-walk Metropolis or the Metropolis-adjusted Langevin algorithm (MALA), due to the fact that it uses local geometric information of the log target density function to obtain global proposals. (Roberts et al., 1997; Roberts and Rosenthal, 1998; Beskos et al., 2013; Neal, 2011). The favorable scalability led to the wide use of HMC in Bayesian data analysis and other fields (Gelman et al., 2013; Neal, 2012; Brooks et al., 2009; Landau and Binder, 2021). When the target distribution is strongly multimodal, however, HMC methods often construct Markov chains that almost never jump between modes (Mangoubi et al., 2018). Moreover, depending on the initial state, the constructed Markov chains may even fail to reach the globally dominant modes that occupy most of the probability mass, thereby misrepresenting

---

*Address for correspondence:* Joonha Park, Department of Mathematics, University of Kansas, 1460 Jayhawk Blvd., Lawrence, KS 66045, USA.

Email: j.park@ku.edu

the target distribution. The strategy of running parallel chains with widely varying initial states may be implemented to increase the chance of finding the dominant modes, but the proportion of chains that settle in different local modes may not accurately reflect the relative probabilities for those modes.

Various strategies aiming at efficient sampling from multimodal target distributions have been developed in the literature. There are a class of methods that use some optimization procedure to find the locations and approximate shapes of the modes of the target posterior and build an MCMC kernel that facilitates jumps between those modes (Andricioaei et al., 2001; Sminchisescu and Welling, 2011; Pompe et al., 2020). Darting Monte Carlo employs an independent Metropolis-Hastings (MH) sampler that proposes a candidate near the known locations of the modes (Andricioaei et al., 2001; Sminchisescu and Welling, 2011). A practical extension was proposed by Ahn et al. (2013) where the independent MH sampler is adaptively tuned using parallel chains at regeneration times. These methods rely on approximations of the target distribution by such models as a mixture of truncated normal distributions whose means and covariances are estimated using the history of the chain. However, these approximations tend to become inaccurate and difficult to implement as the dimension of the space increases.

Tempering is a strategy that utilizes a series of distributions at various *temperature* levels, where the densities are often chosen to be proportional to the target density raised to the power of inverse temperature. Points at low probability density regions are more frequently sampled at high temperature levels. These draws bridge the isolated modes of the target distribution. Simulated tempering constructs a Markov chain targeting a mixture of tempered distributions at different temperature levels (Marinari and Parisi, 1992). Parallel tempering constructs parallel chains, each of which targets a different tempered distribution (Swendsen and Wang, 1986; Geyer, 1991). The tempered transitions method by Neal (1996) concatenates a series of transition kernels so that the sequence of intermediate draws represent the distributions at systematically increasing and decreasing temperature levels. The equi-energy sampler is similar to parallel tempering in that it uses parallel chains targeting distributions at various temperatures, but the state exchange always occurs between the points that belong to the same potential energy band (Kou et al., 2006).

Various tempering approaches have different strengths and drawbacks (see, for example, the discussion section in Neal (1996)). A practical advantage of the tempered transitions method which was not mentioned in Neal (1996), over other tempering methods, is that it can be readily used within the Gibbs sampler settings, where the conditional distribution to draw a sample from changes frequently. Simulated tempering needs careful choice of the mixture weights of the tempered distributions, which may be achieved by adaptive tuning (Wang and Landau, 2001; Atchadé and Liu, 2010). Parallel tempering and equi-energy sampler requires the convergence of the parallel chains to their respective stationary distributions. Either the adaptation of mixture weights for simulated tempering or the convergence of parallel chains for parallel tempering takes time. In contrast, a new sample can be drawn without delay using tempered transitions from each conditional distribution targeted by the Gibbs sampler.

In this paper, we present a hybrid method of tempered transitions and HMC that facilitates frequent mode hops when the target distribution is high-dimensions and multimodal. This method (given in Algorithm 1 in Section 3) can efficiently find unknown locations of local modes in high dimensions using the local geometric information of the negative log target density function, denoted by  $U(x)$ . It simulates the Hamiltonian dynamics for the potential energy function given by  $U(x)$ , while increasing and decreasing the mass of the simulated particle following a certain modulation schedule. The increased mass during the first half of the simulated path supplies the energy necessary to travel across the regions of low probability density between the modes. This approach can be viewed as a tempered transitions method where the transition kernels between the temperature levels are given by simulation of the Hamiltonian dynamics involving a varying mass. Our method, in fact, constructs the same paths as the method proposed in Section 5.5.7 of Neal (2011). However, our formulation of the algorithm in terms of mass scaling, rather than by velocity scaling as presented by Neal (2011), facilitates an in-depth analysis of the Hamiltonian dynamics

in question, which can lead to efficient tuning strategies (see Section 3.3). Our method, which we call tempered Hamiltonian transitions (THT), can be tuned in a way that little or no modification is necessary for varying target distributions in the Gibbs sampler settings. The source codes for the algorithms developed in this paper are available at [https://github.com/joonhap/THT\\_source](https://github.com/joonhap/THT_source).

The rest of the paper is organized as follows. Section 2 discusses why standard Hamiltonian Monte Carlo struggles when the target distribution is multimodal. A toy algorithm (Algorithm 0) is developed using the idea of mass enhancement, and its limitations are discussed. Section 3 explains our main algorithm (tempered Hamiltonian transitions, Algorithm 1) and develops effective tuning methods. We implement the method for mixtures of high-dimensional normal distributions, demonstrating its favorable numerical efficiency. Section 4 considers applications of the method for a sensor network self-localization problem. Section 5 develops an auxiliary strategy that helps when the target distribution has a disconnected support. Section 6 reviews related work and other strategies for sampling from multimodal distributions, and Section 7 concludes with discussion.

## 2 Hamiltonian Monte Carlo and multimodality

In Section 2.1, we review Hamiltonian Monte Carlo and explain why the constructed Markov chains typically mix poorly when the target distribution is multimodal. We will consider a toy algorithm (Algorithm 0) that tackles the identified issue and discuss its limitations in Section 2.2. In Section 2.3, we consider two equivariance properties of the Hamiltonian equations of motion that prove to be useful in developing and understanding our main algorithm (Algorithm 1).

### 2.1 Hamiltonian Monte Carlo

We consider a target density

$$\bar{\pi}(x) = \pi(x) / \int_{\mathcal{X}} \pi(x) dx$$

defined on the space  $\mathcal{X} = \mathbb{R}^d$ . In many practical situations, the unnormalized density  $\pi(x)$  can be evaluated pointwise, but its normalizing constant is unknown. HMC simulates the Hamiltonian dynamics described by the Hamiltonian equations of motion (HEM)

$$\frac{dx}{dt} = \frac{\partial H}{\partial p}, \quad \frac{dp}{dt} = -\frac{\partial H}{\partial x},$$

in order to propose a candidate state for the next state of the constructed Markov chain. Here,  $p$  denotes the *momentum* of the particle, and  $H(x, p)$  denotes the Hamiltonian of the system. The Hamiltonian is defined as the sum of the potential energy  $U(x)$  and the kinetic energy  $K(p)$ ,

$$H(x, p) = U(x) + K(p), \tag{1}$$

where the potential energy is given by

$$U(x) := -\log \pi(x)$$

and the kinetic energy is given by

$$K(p) = \frac{1}{2} p^\top M^{-1} p.$$

The matrix  $M$  is chosen to be positive definite and is interpreted as a generalization of the *mass* of the particle. The Hamiltonian  $H(x, p)$  is understood as the total energy of a particle at location  $x$  having momentum  $p$ . The fact that the normalizing constant for the distribution  $\pi(x)$  is unknown is inconsequential in simulating the Hamiltonian dynamics, because an additive constant in  $H$  does

not affect the HEM. These equations may be equivalently formulated using the *velocity* defined as  $v = M^{-1}p$ . In terms of  $(x, v)$ , the HEM can be expressed as

$$\begin{aligned}\frac{dx}{dt} &= \frac{\partial H}{\partial p} = M^{-1}p = v, \\ \frac{dv}{dt} &= M^{-1} \frac{dp}{dt} = -M^{-1} \frac{\partial U}{\partial x}.\end{aligned}\tag{2}$$

The solution of the HEM is called the Hamiltonian flow and will be denoted by the map  $\Phi_t : (x(0), v(0)) \mapsto (x(t), v(t))$ . The Hamiltonian flow conserves the Hamiltonian, that is,  $H(x(0), v(0)) = H(x(t), v(t))$  for  $\forall t \geq 0$  (Leimkuhler and Reich, 2004). The volume element is also conserved by the Hamiltonian flow:

$$\left| \frac{\partial \Phi_t(x(0), v(0))}{\partial (x(0), v(0))} \right| = 1$$

for any initial condition  $(x(0), v(0))$  and time duration  $t$ , which is known as Liouville's theorem (Liouville, 1838).

Hamiltonian Monte Carlo implicitly targets the extended target distribution  $(x, v) \in \mathbb{R}^{2d}$  whose unnormalized target density is given by

$$\Pi(x, v) = \exp\{-H(x, v)\} = \pi(x) \cdot \exp\left\{-\frac{1}{2}v^\top Mv\right\}.$$

In other words, the velocity variable is independent of  $x$  and is distributed according to the multivariate normal distribution,  $\mathcal{N}(0, M^{-1})$ . If  $X^{(i)}$  denotes the  $i$ -th state of a Markov chain constructed by HMC, a candidate for the  $i+1$ -st state is obtained by numerically simulating the Hamiltonian dynamics for a certain time duration  $t$  starting from  $x(0) = X^{(i)}$  with initial velocity  $v(0)$  drawn from  $\mathcal{N}(0, M^{-1})$ . The numerical simulation, which approximates  $\Phi_t(x(0), v(0))$ , will be denoted by  $\Psi_t(x(0), v(0))$ . The  $x$ -component of  $\Psi_t(x(0), v(0))$  is accepted as the next state of the Markov chain,  $X^{(i+1)}$ , if and only if

$$\Lambda < \exp\left[-H\{\Psi_t(x(0), v(0))\} + H\{x(0), v(0)\}\right] \cdot \left| \frac{\partial \Psi_t(x(0), v(0))}{\partial (x(0), v(0))} \right|\tag{3}$$

where  $\Lambda$  is a  $\text{Uniform}(0, 1)$  random variable drawn independently of all other Monte Carlo draws, such as  $X^{(i)}$  and  $v(0)$ . If (3) is not satisfied,  $X^{(i+1)}$  is equal to  $X^{(i)}$ .

A commonly used numerical approximation method for solving the HEM is called the leapfrog (LF) method (Duane et al., 1987; Leimkuhler and Reich, 2004). One leapfrog step approximately simulates the time evolution of a Hamiltonian system for time duration  $\epsilon$  by alternately updating the velocity and position  $(x, v)$  in half steps as follows:

$$\begin{aligned}v\left(t + \frac{\epsilon}{2}\right) &= v(t) - \frac{\epsilon}{2} \cdot M^{-1} \cdot \nabla U(x(t)) \\ x(t + \epsilon) &= x(t) + \epsilon v\left(t + \frac{\epsilon}{2}\right) \\ v(t + \epsilon) &= v\left(t + \frac{\epsilon}{2}\right) - \frac{\epsilon}{2} \cdot M^{-1} \cdot \nabla U(x(t + \epsilon)).\end{aligned}\tag{4}$$

We will call the time increment unit  $\epsilon$  the leapfrog step size. Since each line in (4) is a translation of either  $v$  or  $x$  by an amount determined by the other variable, it is readily checked that the Jacobian determinant of the leapfrog update is equal to unity. Therefore, the numerical integrator constructed by the leapfrog method preserves the volume element:

$$\left| \frac{\partial \Psi_t(x, v)}{\partial (x, v)} \right| \equiv 1.$$

The numerical stability of the LF method depends on the simulation time step size. In the case of multivariate Gaussian target density with covariance  $\Sigma$ , the numerical error diverges exponentially

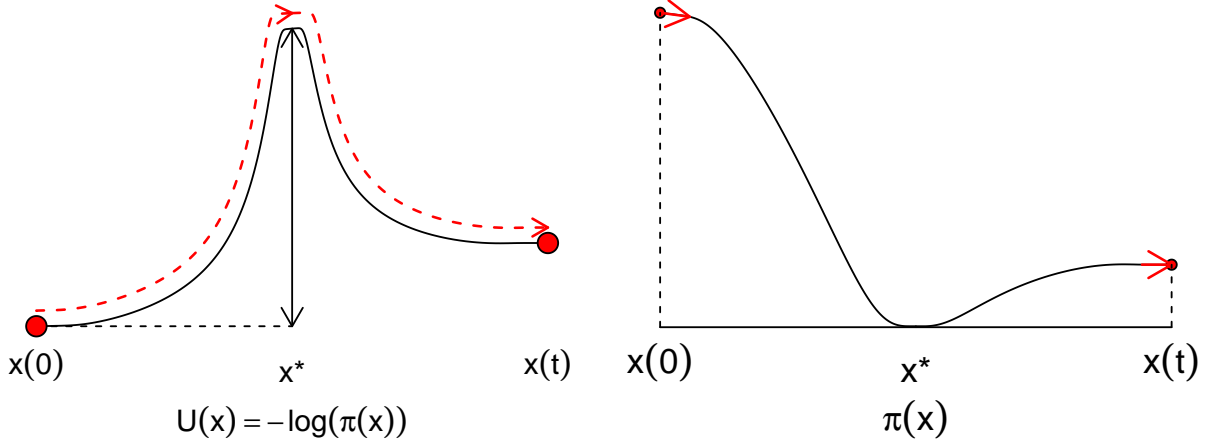


Figure 1: An illustrative diagram of the Hamiltonian path traveling over a region of low target probability density.

fast if and only if the step size  $\epsilon$  is greater than twice the square root of the smallest eigenvalue of  $\Sigma M$ . From this observation, we can speculate that the numerical stability of the LF method is critically dependent on the relative size of its step size to the inverse square root of the largest eigenvalue of the Hessian of the log target density. Provided that the step size is sufficiently small, the numerical solutions obtained by the leapfrog method have long term stability. A consequence is that the Hamiltonian of the numerical solution is close to the initial Hamiltonian for a long period of time:

$$H\{\Psi_t(x(0), v(0))\} \approx H\{x(0), v(0)\}.$$

This long term stability follows from the fact that the LF integrator is symplectic, that is, the map  $\Psi_t$  satisfies

$$\left( \frac{\partial \Psi_t(x, p)}{\partial(x, p)} \right)^\top J^{-1} \left( \frac{\partial \Psi_t(x, p)}{\partial(x, p)} \right) = J^{-1}, \quad \text{where } J = \begin{pmatrix} 0 & I_d \\ -I_d & 0 \end{pmatrix}$$

(Leimkuhler and Reich, 2004). Due to the long term stability and volume preservation, the probability of accepting the candidate  $\Psi_t(x(0), v(0))$  according to the criterion (3) can be made close to one by using sufficiently small LF step size.

When the target distribution is multimodal, HMC typically fails to visit separated modes. Denoting  $(x(s), v(s)) = \Psi_s(x(0), v(0))$ , we have, from

$$H\{x(0), v(0)\} = U\{x(0)\} + K\{v(0)\} \approx H\{x(s), v(s)\} = U\{x(s)\} + K\{v(s)\},$$

that the maximum potential energy increment  $U\{x(s)\} - U\{x(0)\}$  along the path is approximately bounded above by the initial kinetic energy  $K\{v(0)\}$ . Figure 1 schematically illustrates the potential energy  $U(x)$  and the target density  $\pi(x)$  for a path that connects two isolated modes. Since  $v(0)$  is drawn from  $\mathcal{N}(0, M^{-1})$ , we have  $M^{1/2}v(0) \sim \mathcal{N}(0, I)$  where  $M^{1/2}$  is the symmetric square-root matrix of  $M$ , and

$$2K(v(0)) = v(0)^\top M v(0) = \|M^{1/2}v(0)\|_2^2 \sim \chi_d^2,$$

where  $\chi_d^2$  denotes the chi-squared distribution with  $d$  degrees of freedom. Therefore, if there are separated modes in the target distribution  $\pi$ , the probability that a path starting from one mode reaches another has a Chernoff bound

$$\mathcal{P}(K(v(0)) > \Delta) = \mathcal{P}(\chi_d^2 > 2\Delta) \leq \left( \frac{2\Delta}{d} \right)^{d/2} e^{\frac{d}{2} - \Delta}, \quad (5)$$

where  $\Delta$  is the maximum potential energy increment along the path  $\{x(s); 0 \leq s \leq t\}$ ,

$$\Delta = \max_{0 \leq s \leq t} U\{x(s)\} - U\{x(0)\} = -\log \frac{\min_{0 \leq s \leq t} \pi(x(s))}{\pi(x(0))}.$$

The probability (5) is independent of the choice of  $M$  and decreases exponentially fast as  $\Delta$  increases. Due to this fact, standard HMC has a poor global mixing property for highly multimodal target distributions.

## 2.2 Simulation of the Hamiltonian dynamics with enhanced mass

In order to construct Hamiltonian paths that reaches other isolated modes, we may consider simulating the Hamiltonian dynamics with an increased mass. If we increase the mass to  $\tilde{M} := \alpha M$  where  $\alpha > 1$ , the initial kinetic energy increases from  $K(v(0)) = \frac{1}{2}v(0)^\top M v(0)$  to

$$\tilde{K}(v(0)) := \frac{1}{2}v(0)^\top \tilde{M} v(0) = \alpha K(v(0)).$$

With higher initial kinetic energy, the simulated particle may be able to cross high potential energy barriers. We will denote the Hamiltonian with increased mass  $\tilde{M}$  by

$$\tilde{H}(x, v) = U(x) + \tilde{K}(v) = -\log \pi(x) + \frac{1}{2}v^\top \tilde{M} v. \quad (6)$$

A candidate for the next state of the constructed Markov chain can be obtained by a numerical solution to a modified HEM,

$$\begin{aligned} \frac{dx}{dt} &= \tilde{M}^{-1} \tilde{p} = v, \\ \frac{dv}{dt} &= -\tilde{M}^{-1} \frac{\partial U}{\partial x}. \end{aligned} \quad (7)$$

This proposed candidate, denoted by  $\Psi_t(x(0), v(0); \tilde{M})$ , is accepted according to the criterion (3),

$$\Lambda < \exp \left[ -H\{\Psi_t(x(0), v(0); \tilde{M})\} + H\{x(0), v(0)\} \right] \cdot \left| \frac{\partial \Psi_t(x(0), v(0); \tilde{M})}{\partial (x(0), v(0))} \right|. \quad (8)$$

Here  $H(x, v)$  denotes the original Hamiltonian function (1) involving the unchanged mass  $M$ . Since we use the leapfrog method for numerical simulations, the Jacobian determinant for  $\Psi_t(\cdot, \cdot; \tilde{M})$  is equal to the unity. This approach, which we call *mass-enhanced HMC* (Algorithm 0) is a simple algorithmic modification to standard HMC and thus can be readily implemented.

Mass-enhanced HMC (Algorithm 0) uses the recently developed sequential-proposal strategy (Park and Atchadé, 2020). Under this strategy, a collection of candidates are sequentially considered for the next state of the Markov chain, where the acceptance of each candidate is decided using a shared Uniform(0,1) draw. In mass-enhanced HMC, the collection of candidates are obtained by recursively simulating (7) for time increments of  $\tilde{\epsilon}$ . These candidates, denoted by  $\Psi_{n\tilde{\epsilon}}(x(0), v(0); \tilde{M})$ ,  $1 \leq n \leq N$ , are judged based on the criterion (8) where a common Uniform(0,1) draw  $\Lambda$  is used for *all* candidates. This ensures that  $\tilde{\pi}(x)$  is invariant for the constructed Markov chains. The choice of the step size  $\tilde{\epsilon}$  for numerical simulation will be discussed in Section 2.3. The use of the sequential-proposal strategy is critical for mass-enhanced HMC, because, unlike standard HMC, the acceptance probability varies greatly along the path. We can see this from the following equations,

$$\begin{aligned} H\{x(t), v(t)\} &= U(x(t)) + \alpha^{-1} \tilde{K}(v(t)) \\ &= \alpha^{-1} \tilde{H}\{x(t), v(t)\} + (1 - \alpha^{-1})U(x(t)) \\ &\approx \alpha^{-1} \tilde{H}\{x(0), v(0)\} + (1 - \alpha^{-1})U(x(t)) \\ &= H\{x(0), v(0)\} + (1 - \alpha^{-1})\{U(x(t)) - U(x(0))\}, \end{aligned} \quad (9)$$

which say that if  $\alpha \gg 1$ , the amount of change in Hamiltonian  $H$  is close to the change in the potential energy. Since the simulation with enhanced mass  $\tilde{M} = \alpha M$  enables the Hamiltonian



---

**Algorithm 0:** Mass-enhanced HMC using sequential proposals (toy algorithm)

---

**Input** : Potential energy function  $U(x) = -\log \pi(x)$ ; Mass matrix,  $M$ ; Mass enhancement ratio,  $\alpha > 1$ ; Leapfrog step size,  $\tilde{\epsilon}$ ; Number of algorithm iterations,  $I$ ; Maximum number of proposals per iteration,  $N$ ; Number of acceptable states to be found per iteration,  $L$

```
1 Initialize: Set  $X^{(0)}$  arbitrarily
2 for  $i \leftarrow 0:I-1$  do
3   Draw  $\Lambda \sim \text{Uniform}(0,1)$ 
4   Draw  $W_0 \leftarrow \mathcal{N}(0, M^{-1})$  // initial velocity
5   Set  $Y_0 \leftarrow X^{(i)}$ 
6   Set  $X^{(i+1)} \leftarrow X^{(i)}$  // the case where fewer than  $L$  acceptable states were found
7   Set  $n_a \leftarrow 0$  // the number of acceptable candidate states found
8   for  $n \leftarrow 1:N$  do
9      $(Y_n, W_n) \leftarrow \Psi_{\tilde{\epsilon}}(Y_{n-1}, W_{n-1}; \tilde{M}, \tilde{\epsilon})$  obtained by numerically simulating (7) for time  $\tilde{\epsilon}$  with
        mass  $\tilde{M} = \alpha M$  using the leapfrog method with step size  $\tilde{\epsilon}$ .
10    if  $\Lambda < \exp\{-H(Y_n, W_n) + H(Y_0, W_0)\}$  then
11      |  $n_a \leftarrow n_a + 1$ 
12    end
13    if  $n_a = L$  then
14      | Set  $X^{(i+1)} \leftarrow Y_n$ 
15      | break
16    end
17  end
18 end
```

**Output:** A draw of Markov chain,  $(X^{(i)})_{i \in 1:I}$

---

path to reach high potential energy regions that are rarely visited under the stationary distribution  $\bar{\pi}(x)$ , there is large potential energy increase  $U(x(t)) - U(x(0))$  along the path, and the acceptance probability for such  $x(t)$  is exponentially small. The sequential-proposal strategy allows for the simulation to be continued until a low potential energy state is visited and an acceptable candidate is found.

Algorithm 0 can be successful for low-dimensional multimodal target distributions (say  $d \leq 5$ ) or for some special high-dimensional distributions such as a mixture of Gaussian distributions where all mixture components have the same covariance matrix  $\Sigma$  (see Supplementary Section 2.2 for more details). However, in general, mass-enhanced HMC (Algorithm 0) is ineffective in high dimensions, due to the fact that the simulated paths with enhanced mass  $\tilde{M}$  may only rarely visit regions of low potential energy. A potential solution to this issue is to gradually increase and then decrease the mass with which the Hamiltonian dynamics is simulated, so that at the end of the path the particle may settle down at a low potential energy region. This approach is closely related to the idea of tempering within a trajectory, proposed in Section 5.5.7 of Neal (2011). In fact, this approach can be explained as a tempered transitions method where the transition kernels are given by the numerical simulations of the Hamiltonian dynamics. We explain this method, which we call *tempered Hamiltonian transitions* (Algorithm 1), in detail in Section 3 and develop a tuning strategy that enables frequent hops between target density modes.

## 2.3 Two equivariance properties of the Hamiltonian equations of motion

The main method we develop in this paper (Algorithm 1) is closely related to two equivariance properties of the Hamiltonian equations of motion (2). One is a *mass-temperature scale equivariance*

property, which explains the connection between tempering and mass scaling. The other is a *mass–time scale equivariance* property, which gives insights into the choice of the LF step size and the mass scaling schedule for the simulation of the Hamiltonian dynamics. Both of these properties are expressed in terms of transformations of variables in the HEM. Mathematically, this means that the Hamiltonian flow as a function commutes with those variable transformations.

**Mass–temperature scale equivariance.** Tempering is a technique that has an analogy with a statistical mechanical concept called canonical ensemble, which describes a collection of microscopic states of a physical system in constant temperature. In a canonical ensemble, a certain configuration of the system denoted by  $x$  occurs with probability proportional to  $e^{-U(x)/T}$  where  $T$  denotes the temperature. Thus increasing the temperature from  $T = 1$  to  $T = \alpha > 1$  is equivalent to scaling down the potential energy function from  $U(x)$  to

$$\check{U}(x) := \alpha^{-1}U(x)$$

in terms of the distribution of the microscopic states. The HEM (2) for this  $\check{U}(x)$  are given by

$$\begin{aligned} \frac{dx}{dt} &= v, \\ \frac{dv}{dt} &= -M^{-1}\frac{\partial\check{U}}{\partial x} = -M^{-1}\alpha^{-1}\frac{\partial U}{\partial x} = -(\alpha M)^{-1}\frac{\partial U}{\partial x}. \end{aligned} \tag{10}$$

Since the above equations are identical to (7) with  $\tilde{M} = \alpha M$ , the HEM with temperature  $T = \alpha$  and mass  $M$  is equivalent to that with  $T = 1$  and  $\tilde{M} = \alpha M$ :

$$(M, T = \alpha) \quad \underset{\text{equivalent}}{\longleftrightarrow} \quad (\tilde{M} = \alpha M, T = 1). \tag{11}$$

With increasing  $\alpha$ , the degree of multimodality of the target density  $\check{\pi}(x) \propto e^{-\check{U}(x)} \propto \pi^{\alpha^{-1}}(x)$  reduces, so  $\check{\pi}(x)$  is often easier to sample from using MCMC methods.

**Mass–time scale equivariance.** We next consider a transformation

$$\begin{aligned} d\tilde{t} &:= \alpha^{1/2}dt, \\ \tilde{v}(\tilde{t}) &:= \alpha^{-1/2}v(t). \end{aligned} \tag{12}$$

If  $(x(t), v(t))$  satisfies the HEM (2), then  $(x(\tilde{t}), \tilde{v}(\tilde{t}))$  satisfies, where  $x(\tilde{t})$  denotes the position of the particle at the transformed time  $\tilde{t}$ ,

$$\begin{aligned} \frac{dx}{d\tilde{t}} &= \alpha^{-1/2}\frac{dx}{dt} = \alpha^{-1/2}v = \tilde{v}, \\ \frac{d\tilde{v}}{d\tilde{t}} &= \frac{\alpha^{-1/2}}{\alpha^{1/2}}\frac{dv}{dt} = \alpha^{-1}M^{-1}\frac{\partial U}{\partial x} = \tilde{M}^{-1}\frac{\partial U}{\partial x}. \end{aligned} \tag{13}$$

Thus the transformed variables  $(x(\tilde{t}), \tilde{v}(\tilde{t}))$  is a solution to the HEM with mass  $\tilde{M}$ , and we have a mass–time scale equivariance

$$(dt, v, M) \quad \underset{\text{equivalent}}{\longleftrightarrow} \quad (d\tilde{t} = \alpha^{1/2}dt, \tilde{v} = \alpha^{-1/2}v, \tilde{M} = \alpha M). \tag{14}$$

This equivariance property implies that the discrete-time numerical simulation described by (4) with the LF step size given by

$$\tilde{\epsilon} = \alpha^{1/2}\epsilon$$



and the initial state  $(x(0), \tilde{v}(0)) = (x(0), \alpha^{-1/2}v(0))$  and mass  $\tilde{M}$  constructs the same path as the LF numerical simulation with step size  $\epsilon$ , initial state  $(x(0), v(0))$ , and mass  $M$ . This can be checked explicitly by the following equations:

$$\begin{aligned}
\tilde{v}\left(\tilde{t} + \frac{\tilde{\epsilon}}{2}\right) &= \alpha^{-1/2}v\left(t + \frac{\epsilon}{2}\right) = \alpha^{-1/2}v(t) - \alpha^{-1/2}\frac{\epsilon}{2}M^{-1}\nabla U(x(t)) \\
&= \tilde{v}(\tilde{t}) - \frac{\tilde{\epsilon}}{2}(\alpha M)^{-1}\nabla U(x(\tilde{t})), \\
x(\tilde{t} + \tilde{\epsilon}) &= x(t + \epsilon) = x(t) + \epsilon v\left(t + \frac{\epsilon}{2}\right) \\
&= x(t) + \alpha^{-1/2}\tilde{\epsilon}\alpha^{1/2}\tilde{v}\left(\tilde{t} + \frac{\tilde{\epsilon}}{2}\right) \\
&= x(\tilde{t}) + \tilde{\epsilon}\tilde{v}\left(\tilde{t} + \frac{\tilde{\epsilon}}{2}\right), \\
\tilde{v}(\tilde{t} + \tilde{\epsilon}) &= \alpha^{-1/2}v(t + \epsilon) = \alpha^{-1/2}v\left(t + \frac{\epsilon}{2}\right) - \alpha^{-1/2}\frac{\epsilon}{2}M^{-1}\nabla U(x(t + \epsilon)) \\
&= \tilde{v}\left(\tilde{t} + \frac{\tilde{\epsilon}}{2}\right) - \frac{\tilde{\epsilon}}{2}(\alpha M)^{-1}\nabla U(x(\tilde{t} + \tilde{\epsilon})).
\end{aligned}$$

Furthermore, since the transformation (12) is one-to-one and onto, the numerical simulation of  $(x(\tilde{t}), \tilde{v}(\tilde{t}))$  is stable if and only if the numerical simulation of  $(x(t), v(t))$  is stable.

## 3 Tempered Hamiltonian transitions

### 3.1 Tempering within a trajectory (Neal, 2011)

Neal (2011, Section 5.5.7) proposed an HMC method for multimodal target distributions where tempering is implemented within each constructed trajectory. This approach increases the velocity by a certain multiplicative factor (say  $\xi$ ) after every leapfrog step for a certain number of steps and then decreases the velocity by the same factor for the same number of steps. During the first half of the trajectory, the Hamiltonian gradually increases, and it becomes possible to escape from a local basin of the function  $U(x)$  containing the current state of the constructed Markov chain. During the second half, the Hamiltonian gradually decreases, so that the trajectory settles down at a possibly different local basin. The end point of the trajectory is considered as a candidate for the next state of the Markov chain.

The velocity scaling approach by Neal (2011) can be alternatively formulated in terms of mass scaling, using the mass-time scale equivariance (14). Let  $t$  be a continuous time variable increasing linearly with the number of leapfrog steps, such that a leapfrog step of size  $\epsilon$  advances the time by  $\Delta t = \epsilon$ . Let  $\eta(t)$  be the accumulation of the log of the velocity multiplication factors by time  $t$ , so that  $\Delta\eta = \pm \log \xi$  after each leapfrog step. This velocity scaling may be viewed as a discretization of the continuous-time equation

$$dv = v d\eta = v \frac{d\eta}{dt} dt. \quad (15)$$

Thus Neal's trajectory is a numerical solution to the equations

$$\begin{aligned}
\frac{dx}{dt} &= v, \\
\frac{dv}{dt} &= -M^{-1}\frac{\partial U}{\partial x} + v \frac{d\eta}{dt}.
\end{aligned} \quad (16)$$

Now consider a transformation of the time scale and velocity given by

$$d\tilde{t} := e^{\eta(t)} dt, \quad \tilde{v} := e^{-\eta(t)} v. \quad (17)$$

The new variables  $(x(\tilde{t}), \tilde{v}(\tilde{t}))$  satisfy

$$\begin{aligned}
\frac{dx}{d\tilde{t}} &= e^{-\eta}v = \tilde{v}, \\
\frac{d\tilde{v}}{d\tilde{t}} &= e^{-\eta}\frac{d}{dt}(e^{-\eta}v) \\
&= -e^{-2\eta}\frac{d\eta}{dt}v + e^{-2\eta}\frac{dv}{dt} \\
&= -e^{-2\eta}\frac{d\eta}{dt}v + e^{-2\eta}\left(-M^{-1}\frac{\partial U}{\partial x} + v\frac{d\eta}{dt}\right) \\
&= -(e^{2\eta}M)^{-1}\frac{\partial U}{\partial x}.
\end{aligned} \tag{18}$$

Thus  $(x(\tilde{t}), \tilde{v}(\tilde{t}))$  satisfy the HEM with time-varying mass  $e^{2\eta(t)}M$ . Hereafter, we will write

$$\alpha := e^{2\eta}. \tag{19}$$

We note that the dynamics described by (18) can be viewed as tempering within a trajectory, using the mass–temperature scale equivariance (11).

## 3.2 Tempered Hamiltonian transitions with sequential proposals

We develop our main algorithm (tempered Hamiltonian transitions, Algorithm 1). Our method differs from Neal (2011)’s approach in two ways. First, our method modulates the Hamiltonian dynamics by changing the mass, not by directly scaling the velocity. This alternative approach enables developing an efficient tuning strategy, which is discussed in Section 3.3. Second, we extend Neal (2011)’s method such that points other than the end point of the simulated trajectory can be considered as a candidate for the next state of the constructed Markov chain. A seemingly similar idea was mentioned in Neal (2011), but details were not given.

Our extension involves the sequential-proposal strategy described in Park and Atchadé (2020). This sequential-proposal strategy can be employed to extend a broad class of MCMC methods including HMC and some variants of the bouncy particle sampler (Vanetti et al., 2017; Bouchard-Côté et al., 2018; Park and Atchadé, 2020). This class of methods target an extended density  $\Pi(x, v) = \bar{\pi}(x)\psi(v; x)$  defined on  $\mathsf{X} \times \mathsf{V} = \mathbb{R}^{2d}$ , where the original target density  $\bar{\pi}(x)$  is the marginal over  $v$ . The conditional density  $\psi(v; x)$  can depend on  $x$  in general, but we will only consider the cases where it is independent of  $x$  and denote it by  $\psi(v)$ . Candidates for the next state of the Markov chain are obtained by recursively applying a deterministic map  $\mathcal{S}_\tau : \mathsf{X} \times \mathsf{V} \rightarrow \mathsf{X} \times \mathsf{V}$ , starting from the initial position-velocity pair given by  $(X^{(i)}, v(0))$ . The initial velocity  $v(0)$  is drawn from  $\psi(v)$ . The subscript  $\tau$  denotes a parameter for the recursive proposal map  $\mathcal{S}_\tau$ . For HMC,  $\mathcal{S}_\tau$  is given by a numerically simulated Hamiltonian flow for time duration  $\tau$ . The proposal map  $\mathcal{S}_\tau$  must satisfy the *reversibility condition*, which says that there exists a collection of self-inverse *velocity reflection* operators  $\mathcal{R}_x$ ,  $x \in \mathsf{X}$ , such that the velocity distribution  $\psi(v)$  is preserved,

$$\frac{\psi(\mathcal{R}_x v)}{\psi(v)} \left| \frac{\partial \mathcal{R}_x v}{\partial v} \right| = 1, \tag{20}$$

and the following equation holds,

$$\mathcal{T} \circ \mathcal{S}_\tau \circ \mathcal{T} \circ \mathcal{S}_\tau = \text{id}_{\mathsf{X} \times \mathsf{V}}, \tag{21}$$

where we write  $\mathcal{T}(x, v) := (x, \mathcal{R}_x v)$ . Here,  $\text{id}_{\mathsf{X} \times \mathsf{V}}$  denotes the identity map on the product space  $\mathsf{X} \times \mathsf{V}$ . In standard HMC, the reversibility condition is satisfied with  $\mathcal{R}_x \equiv -\text{id}_{\mathsf{V}}$ . The  $n$ -th proposal  $(Y_n, W_n) = \mathcal{S}_\tau^n(X^{(i)}, V)$  is deemed *acceptable* if and only if

$$\Lambda < \frac{\Pi(Y_n, W_n)}{\Pi(X^{(i)}, V)} \left| \frac{\partial(Y_n, W_n)}{\partial(X^{(i)}, V)} \right|, \tag{22}$$

---

**Algorithm 1:** Tempered Hamiltonian transitions

---

**Input** : Potential energy function  $U(x) = -\log \pi(x)$ ; Mass matrix,  $M$ ; Mass scaling schedule,  $\{\alpha_k = e^{2\eta_k}; k \in \mathbb{Z}/2\}$  and its period  $K$ ; Discrete distribution  $\psi_K(k)$  on  $0 : (K-1)$ ; Baseline leapfrog step size,  $\epsilon$ ; Simulation time scale coefficient,  $a$ ; Number of algorithm iterations,  $I$ ; Maximum number of candidate proposals per iteration step,  $N$ ; Number of acceptable states to be found per iteration step,  $L$

- 1 **Initialize:** Set  $X^{(0)}$  arbitrarily
- 2 **for**  $i \leftarrow 0 : I-1$  **do**
- 3     Draw  $\Lambda \sim \text{Uniform}(0, 1)$
- 4     Draw  $k_0 \sim \psi_K(k)$
- 5     Draw  $\tilde{v}(0) \leftarrow \mathcal{N}(0, \alpha_{k_0}^{-1} M^{-1})$      // initial velocity
- 6     Set  $Y_0 \leftarrow X^{(i)}$  and  $W_0 \leftarrow \tilde{v}(0)$
- 7     Set  $H_0 \leftarrow H(Y_0, k_0, W_0)$  where  $H$  is defined in (24)
- 8     Set  $X^{(i+1)} \leftarrow X^{(i)}$      // the case where fewer than  $L$  acceptable states were found
- 9     Set  $n_a \leftarrow 0$      // the number of acceptable candidate states found
- 10    **for**  $n \leftarrow 1 : N$  **do**
- 11     Set  $\tilde{\epsilon} \leftarrow \epsilon \cdot \alpha_{k_0+n-\frac{1}{2}}^a$
- 12      $(Y_n, W_n) \leftarrow \Psi_{\tilde{\epsilon}}(Y_{n-1}, W_{n-1}; \alpha_{k_0+n-\frac{1}{2}} M, \tilde{\epsilon})$  obtained by carrying out one leapfrog step (4) from  $(Y_{n-1}, W_{n-1})$  with mass  $\alpha_{k_0+n-\frac{1}{2}} M$  and step size  $\tilde{\epsilon}$
- 13     **if**  $\Lambda < \exp\{-H(Y_n, k_0+n, W_n) + H(Y_0, k_0, W_0)\}$  **then**
- 14          $n_a \leftarrow n_a + 1$
- 15     **end**
- 16     **if**  $n_a = L$  **then**
- 17         Set  $X^{(i+1)} \leftarrow Y_n$
- 18         **break**
- 19     **end**
- 20    **end**
- 21 **end**

**Output:** A draw of Markov chain,  $(X^{(i)})_{i \in 1:I}$

---

where  $\Lambda$  is a  $\text{Uniform}(0,1)$  random number drawn once per iteration step. The  $L$ -th acceptable candidate is taken for the next state of the Markov chain, if it exists among the first  $N$  proposed candidates, where  $L$  and  $N$  are tuning parameters in the algorithm. If not,  $X^{(i+1)}$  is equal to  $X^{(i)}$ .

Our method carries out a leapfrog simulation step with varying mass for the recursive proposal map  $\mathcal{S}_\tau$ . The pseudocode of this method is given in Algorithm 1. It uses a periodic sequence of mass scale factors indexed by integers and half-integers,  $\{\alpha_k > 0; k \in \mathbb{Z}/2\}$ . We denote the period of the sequence by  $K \in \mathbb{Z}_+$ , so that  $\alpha_k = \alpha_{k+K}$  for all  $k \in \mathbb{Z}/2$ . Following (19), we write  $\eta_k := \frac{1}{2} \log \alpha_k$  for all  $k$ . The sequence of mass scale factors must be symmetric about zero (i.e.,  $\alpha_k = \alpha_{-k}$ ,  $\forall k \in \mathbb{Z}/2$ ) in order to ensure detailed balance of the constructed Markov chains. The mass scale factors with integer indices are used to scale the variance of the velocity distribution. Formally, we extend the auxiliary variable from  $v$  to  $(k, \tilde{v})$ , where  $k$  is an integer modulo  $K$  and  $\tilde{v} \in \mathbb{R}^d$ . The extended target density is given by

$$\Pi(x, k, \tilde{v}) := \bar{\pi}(x) \psi_K(k) \phi(\tilde{v}; 0, \alpha_k^{-1} M^{-1}),$$

where  $\phi(\cdot; 0, \alpha_k^{-1} M^{-1})$  denotes the multivariate normal density with mean 0 and variance  $\alpha_k^{-1} M^{-1}$ . The discrete distribution  $\psi_K(k)$  defined on the space of integers modulo  $K$  must be symmetric, that is,  $\psi_K(k) = \psi_K(-k)$  for all  $k \pmod{K}$ . The initial value of  $k$  and the initial velocity for each iteration step are drawn from the extended target density:

$$k_0 \sim \psi_K(k), \quad \tilde{v}(0) \sim \mathcal{N}(0, \alpha_{k_0}^{-1} M^{-1}).$$

Mass scale factors  $\alpha_k$  indexed by half-integer  $k$  are used to scale the mass used in the simulation of the Hamiltonian dynamics and the LF step size. The recursive proposal map  $\mathcal{S}$  is given by

$$\begin{aligned}\mathcal{S}(x, k, \tilde{v}) &:= (x'', k+1, \tilde{v}''), \text{ where} \\ \tilde{v}' &= \tilde{v} - \frac{\tilde{\epsilon}}{2} \{\alpha_{k+\frac{1}{2}} M\}^{-1} \nabla U(x) \\ x'' &= x + \tilde{\epsilon} \tilde{v}' \\ \tilde{v}'' &= \tilde{v}' - \frac{\tilde{\epsilon}}{2} \{\alpha_{k+\frac{1}{2}} M\}^{-1} \nabla U(x'').\end{aligned}\tag{23}$$

In other words,  $\mathcal{S}$  increases  $k$  by one modulo  $K$  and carries out one LF step with mass  $\alpha_{k+\frac{1}{2}} M$  and time increment  $\tilde{\epsilon}$ . We propose to use the LF step size given by  $\tilde{\epsilon} := \alpha_{k+\frac{1}{2}}^a \epsilon$ , where the choice of the constant  $a$  will be discussed in Section 3.3. The  $n$ -th proposed candidate is given by

$$(Y_n, k_0 + n, W_n) = \mathcal{S}^n(X^{(i)}, k_0, \tilde{v}(0)).$$

The map  $\mathcal{S}$  has unit Jacobian determinant, so the acceptability criterion (22) can be expressed as

$$\Lambda < e^{-H(Y_n, k_0+n, W_n) + H(X^{(i)}, k_0, \tilde{v}(0))},$$

where the extended Hamiltonian is given by

$$H(x, k, \tilde{v}) = U(x) - \log \psi_K(k) + \frac{1}{2} \tilde{v}^\top \{\alpha_k M\} \tilde{v} - \frac{1}{2} \log \det \{\alpha_k M\}.\tag{24}$$

We note that Algorithm 1 behaves the same way as the method proposed by Neal (2011) in Section 5.5.7 if the distribution  $\psi_K(k)$  puts all its mass at  $k = 0$ , the mass scaling schedule is given by a triangular function

$$\eta_k = \begin{cases} \xi \cdot k, & \text{if } 0 \leq k \leq K/2 \\ \xi \cdot (K - k), & \text{if } K/2 < k \leq K, \end{cases}$$

and  $N = L = 1$ .

The following Lemma 1 and Proposition 1 shows that Algorithm 1 constructs a reversible Markov chain with invariant density  $\bar{\pi}(x)$ .

**Lemma 1.** *The map  $\mathcal{S}$  defined by (23) satisfies the reversibility condition (20) and (21) with the velocity reflection operator given by*

$$\mathcal{R}_x(k, \tilde{v}) = (-k, -\tilde{v}), \quad \forall x, k, \tilde{v}.$$

*Proof.* Since both  $\psi_K(k)$  and  $\phi(\tilde{v}; 0, \alpha_k^{-1} M^{-1})$  are symmetric about zero, we have  $\psi(\mathcal{R}_x(k, \tilde{v})) = \psi(k, \tilde{v})$  where  $\psi(k, \tilde{v}) := \psi_K(k) \phi(\tilde{v}, \alpha_k^{-1} M^{-1})$ . Thus the measure-preserving condition (20) is satisfied. Next we check (21). If we write  $\mathcal{S}(x, k, \tilde{v}) = (x'', k+1, \tilde{v}'')$ , we have

$$\mathcal{T} \circ \mathcal{S}(x, k, \tilde{v}) = \mathcal{T}(x'', k+1, \tilde{v}'') = (x'', -k-1, -\tilde{v}'').$$

Now observe that that  $\mathcal{S}(x'', -k-1, -\tilde{v}'')$  is obtained by carrying out one LF step from the initial position  $x''$  and initial velocity  $-\tilde{v}''$  with mass  $\alpha_{-k-1+\frac{1}{2}} M$  and time step  $\tilde{\epsilon} = \alpha_{-k-1+\frac{1}{2}}^a \epsilon$ . Since  $\alpha_{-k-\frac{1}{2}} = \alpha_{k+\frac{1}{2}}$  due to the symmetry of  $\{\alpha_k\}$ , we have

$$\begin{aligned}\mathcal{S}(x'', -k-1, -\tilde{v}'') &:= (x, -k, -\tilde{v}), \text{ where} \\ -\tilde{v}' &= -\tilde{v}'' - \frac{\tilde{\epsilon}}{2} \{\alpha_{k+\frac{1}{2}} M\}^{-1} \nabla U(x'') \\ x &= x'' + \tilde{\epsilon}(-\tilde{v}') \\ -\tilde{v} &= -\tilde{v}' - \frac{\tilde{\epsilon}}{2} \{\alpha_{k+\frac{1}{2}} M\}^{-1} \nabla U(x).\end{aligned}$$

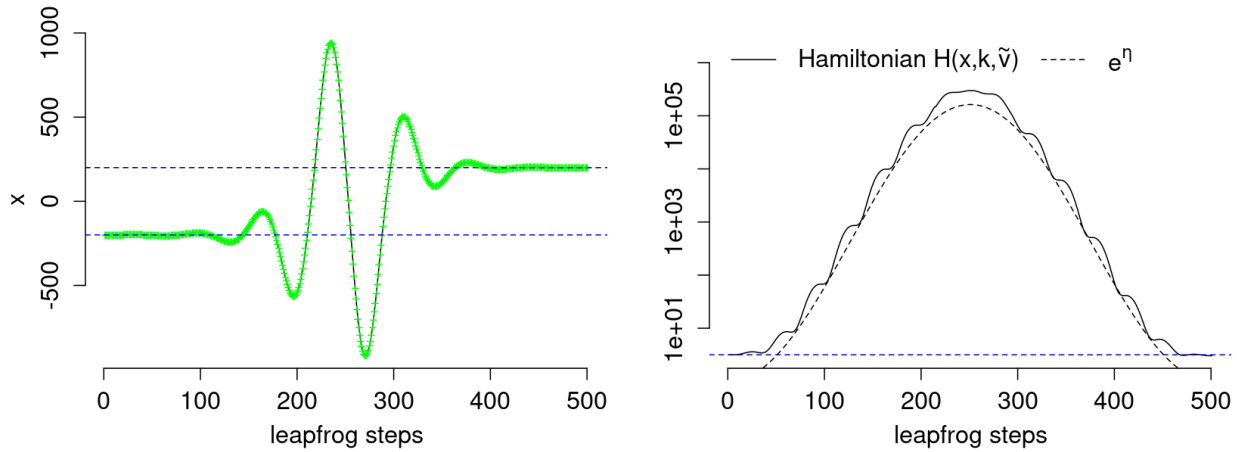


Figure 2: An example trajectory where the mass is altered while the Hamiltonian dynamics is simulated. The target density is the mixture of two one-dimensional Gaussians,  $\frac{1}{2}\phi(x; -200, 1^2) + \frac{1}{2}\phi(x; 200, 1^2)$ . The centers of the two density components are shown by the two horizontal dashed lines. The Hamiltonian  $H(x, k, \tilde{v}) = U(x) + \frac{1}{2}\tilde{v}^\top \{\alpha_k M\} \tilde{v} - \frac{1}{2} \log \det \{\alpha_k M\}$  and the square root of the mass scale factor,  $\alpha_k^{1/2}$ , are shown on the right panel.

In other words, after the action of  $\mathcal{T}$ , the application of the map  $\mathcal{S}$  reverses the previous application of  $\mathcal{S}$ , so that we have  $\mathcal{S}(x'', -k-1, -\tilde{v}'') = (x, -k, -\tilde{v})$ . Finally by applying  $\mathcal{T}$  again, we have

$$\mathcal{T} \circ \mathcal{S} \circ \mathcal{T} \circ \mathcal{S}(x, k, \tilde{v}) = \mathcal{T}(x, -k, -\tilde{v}) = (x, k, \tilde{v}).$$

□

**Proposition 1.** *Algorithm 1 constructs a reversible Markov chain  $\{X^{(i)}\}$  with respect to the target density  $\bar{\pi}(x)$ .*

*Proof.* Lemma 1 shows that Algorithm 1 belongs to the class of sequential-proposal MCMC algorithms targeting the extended distribution  $\Pi(x, k, \tilde{v})$ . Thus Proposition 2 in Park and Atchadé (2020) shows that  $\{X^{(i)}\}$  is reversible with respect to  $\bar{\pi}(x)$ . □

The following example demonstrates how Algorithm 1 works for a bimodal distribution.

**Example 3.1** Consider the target distribution given by a mixture of two Gaussian components

$$\frac{1}{2}\mathcal{N}(-200, 1^2) + \frac{1}{2}\mathcal{N}(200, 1^2).$$

Figure 2 shows an example of numerically simulated Hamiltonian path for Algorithm 1. This path starts at a point drawn from one of the two components,  $\mathcal{N}(-200, 1^2)$ . The sequence of mass scale factor was given by  $\alpha_k = \exp[12\{1 - \cos(2\pi k/500)\}]$ . As  $\alpha_k$  increases, the simulated path visits regions far from the initial mode. During the second half of the path, total amount of energy, or the Hamiltonian, of the simulated particle decreases, and the path settles down near one of the two density modes, which in this case is one that is different from the initial mode. The right panel of Figure 2 shows the extended Hamiltonian along this path. The increment in the Hamiltonian at the end of the trajectory is close to zero ( $\approx -0.13$ ). The fact that the Hamiltonian is almost exactly preserved at the end of one cycle may seem surprising, given that the Hamiltonian increases and decreases at an exponential scale during the trajectory. In fact, if the sequence of mass scaling factors  $\{\alpha_k\}$  and the leapfrog step size are not tuned adequately, the Hamiltonian would not decrease during the second half of the trajectory by the same amount it increased during the first half, so the acceptance probability can be exponentially small. A physical intuition for this phenomenon was discussed in Neal (2011, Section 5.5.7) and Neal (1996, Section 3.3). We will examine numerically efficient tuning strategies for various parameters in Section 3.3. □

### 3.3 Tuning strategy for Algorithm 1

#### 3.3.1 Theoretical and numerical insight gained from the case $U(x) \propto \|x\|^\gamma$

In this section, we aim to develop efficient tuning strategies for the input parameters in Algorithm 1, such as  $\{\alpha_k\}$ ,  $\epsilon$ , and  $\psi_K(k)$ . We will consider target density  $\pi$  of the form

$$-\log \pi(x) = U(x) \propto \|x\|_B^\gamma := (x^\top Bx)^{\gamma/2}, \quad \gamma > 0$$

where  $B$  is a symmetric positive definite matrix, for the purpose of developing insight into the behavior of the simulated paths. A key aim is to ensure that the increment in the Hamiltonian  $H(x, k, \tilde{v})$  is close to zero at the end of the simulated paths. Note that the HEM (18)

$$\frac{dx}{d\tilde{t}} = \tilde{v}, \quad \frac{d\tilde{v}}{d\tilde{t}} = -(e^{2\eta}M)^{-1} \frac{\partial U}{\partial x},$$

is written with respect to  $\tilde{t}$ . We will consider a time scale change

$$dt = e^{-2a\eta} d\tilde{t} \tag{25}$$

and transformed variables

$$\bar{v} := \tilde{v} \cdot e^{a\eta}, \quad \bar{x} := x \cdot e^{-a\eta}, \tag{26}$$

where  $a$  is some constant. Note that in Section 3.1, we considered a time change  $dt = e^{-\eta} d\tilde{t}$ , which linked (16) and (18), but here we consider a possibly different relative time scale between  $dt$  and  $d\tilde{t}$ . We will show that when  $a = \frac{2}{\gamma+2}$ , the solutions for  $\bar{v}(t)$  and  $\bar{x}(t)$  are oscillatory with approximately constant amplitudes and frequencies, provided that  $\eta$  is slowly varying. This result will imply that the increment in the extended Hamiltonian (24) is approximately zero.

For our analysis, we consider continuous-time equations of motion that involve continuously varying  $\eta(t)$  that satisfies

$$\eta(0) = \eta_{k_0} = \frac{1}{2} \log \alpha_{k_0} \quad \text{and} \quad \eta(n\epsilon) = \eta_{k_0+n} = \frac{1}{2} \log \alpha_{k_0+n},$$

where  $k_0$  is the initial value of  $k$  drawn from  $\psi_K$  for a given iteration step of Algorithm 1. The recursive proposal map  $\mathcal{S}$  in (23) is designed to advance time by  $\Delta t = \epsilon$ , so that  $t$  grows linearly with the number of leapfrog steps. Since  $d\tilde{t} = e^{2a\eta} dt$ , the numerical simulation for  $(x(\tilde{t}), \tilde{v}(\tilde{t}))$  is carried out by making a leapfrog step with step size

$$\tilde{\epsilon} = \epsilon \cdot e^{2a\eta_{k_0+n+\frac{1}{2}}}.$$

for time advancement from  $t = n\epsilon$  to  $t = (n+1)\epsilon$ . In this paper, we consider mass scaling schedules of the form

$$\eta(t) = \eta_* \sin(\omega t + \varphi) + c_\eta \tag{27}$$

for some  $\eta_* > 0$  and  $c_\eta \in \mathbb{R}$ . We will consider slowly varying  $\eta(t)$ , that is,  $\max |d\eta/dt| = \eta_* \omega \ll 1$ . Since  $K$  is the period of the mass scaling schedule, we have  $\omega = \frac{2\pi}{K\epsilon}$ .

The next proposition will be used to show that  $\bar{x}(t)$  and  $\bar{v}(t)$  have almost constant orders of magnitude for the simulated Hamiltonian paths.

**Proposition 2.** *Consider a potential function  $U(x) \propto \|x\|_B^\gamma = (x^\top Bx)^{\gamma/2}$  where  $\gamma > 0$  and  $B$  is a symmetric positive definite matrix. Then  $\bar{v} := \tilde{v} \cdot e^{a\eta}$  and  $\bar{x} := x \cdot e^{-a\eta}$  satisfy the following equations*

$$\begin{aligned} \frac{d\bar{x}}{dt} &= \bar{v} - \bar{x} \cdot a \frac{d\eta}{dt}, \\ \frac{d\bar{v}}{dt} &= -e^{\{a(\gamma+2)-2\}\eta} M^{-1} \nabla U(\bar{x}) + \bar{v} \cdot a \frac{d\eta}{dt}. \end{aligned} \tag{28}$$

*Proof.* We have

$$\nabla U(x) = \nabla(x^\top Bx)^{\gamma/2} = \frac{\gamma}{2} \cdot (x^\top Bx)^{\frac{\gamma}{2}-1} \cdot 2Bx = \gamma \|x\|_B^{\gamma-2} Bx.$$

From (18), we see that  $(\bar{x}(t), \bar{v}(t))$  satisfy the differential equations

$$\begin{aligned} \frac{d\bar{x}}{dt} &= \frac{dx}{dt} e^{-a\eta} - x \cdot a \frac{d\eta}{dt} e^{-a\eta} = \left( e^{2a\eta} \frac{dx}{dt} \right) \cdot e^{-a\eta} - \bar{x} \cdot a \frac{d\eta}{dt} = \bar{v} - \bar{x} \cdot a \frac{d\eta}{dt}, \\ \frac{d\bar{v}}{dt} &= \frac{d\tilde{v}}{dt} \cdot e^{a\eta} + \tilde{v} \cdot a \frac{d\eta}{dt} e^{a\eta} \\ &= e^{2a\eta} \cdot \{ -(e^{2\eta} M)^{-1} \nabla U(x) \} \cdot e^{a\eta} + \bar{v} \cdot a \frac{d\eta}{dt} \\ &= -e^{(3a-2)\eta} M^{-1} \gamma \|x\|_B^{\gamma-2} Bx + \bar{v} \cdot a \frac{d\eta}{dt} \\ &= -e^{\{a(\gamma+2)-2\}\eta} M^{-1} \gamma \|\bar{x}\|_B^{\gamma-2} B\bar{x} + \bar{v} \cdot a \frac{d\eta}{dt} \\ &= -e^{\{a(\gamma+2)-2\}\eta} M^{-1} \nabla U(\bar{x}) + \bar{v} \cdot a \frac{d\eta}{dt}. \end{aligned}$$

□

The next corollary considers the special case  $\gamma = 2$ . For the sake of mathematical convenience, we assume that  $\frac{d\eta}{dt}$  is constant in Corollary 1, which is almost true in local time windows since  $\eta$  is slowly varying.

**Corollary 1.** *Consider the potential function given by  $U(x) = \|x\|_B^2 = x^\top Bx$ . Suppose that  $\frac{d\eta}{dt}$  is constant. Then  $\bar{v} := \tilde{v} \cdot e^{a\eta}$  and  $\bar{x} := x \cdot e^{-a\eta}$  are linear combinations of sinusoidal functions with constant amplitude and constant frequency, provided that*

$$2\lambda_{\min}(M^{-1}B) > a^2 \left( \frac{d\eta}{dt} \right)^2,$$

where  $\lambda_{\min}(M^{-1}B)$  signifies the smallest eigenvalue of  $M^{-1}B$ , which is positive.

*Proof.* From Proposition 2 we know that  $(\bar{x}(t), \bar{v}(t))$  solves linear differential equations

$$\frac{d}{dt} \begin{pmatrix} \bar{x} \\ \bar{v} \end{pmatrix} = \begin{pmatrix} -a \frac{d\eta}{dt} I & I \\ -2M^{-1}B & a \frac{d\eta}{dt} I \end{pmatrix} \begin{pmatrix} \bar{x} \\ \bar{v} \end{pmatrix}. \quad (29)$$

Since  $B$  is symmetric and positive definite, the matrix  $M^{-1}B = M^{-1}B^{1/2}B^{1/2}$  has the same set of eigenvalues as  $B^{1/2}M^{-1}B^{1/2}$ , which is positive definite. Therefore all eigenvalues of  $M^{-1}B$  are positive. Let  $\lambda_1, \dots, \lambda_d$  be the eigenvalues of  $M^{-1}B$ , with associated eigenvectors  $u_1, \dots, u_d$ . It can be readily checked that the eigenvalues of the rate matrix in (1) are given by  $\pm \sqrt{-2\lambda_j + a^2(d\eta/dt)^2}$  with associated eigenvectors

$$\left( u^\top, \left\{ a \frac{d\eta}{dt} \pm \sqrt{-2\lambda_j + a^2 \left( \frac{d\eta}{dt} \right)^2} \right\} u^\top \right)^\top.$$

All of these eigenvalues are purely imaginary if  $2\lambda_{\min}(M^{-1}B) > a^2 \left( \frac{d\eta}{dt} \right)^2$ . Therefore the solutions of (1) are linear combinations of sinusoidal functions with frequencies  $\sqrt{2\lambda_j - a^2(d\eta/dt)^2}$ ,  $j = 1, \dots, d$ . □



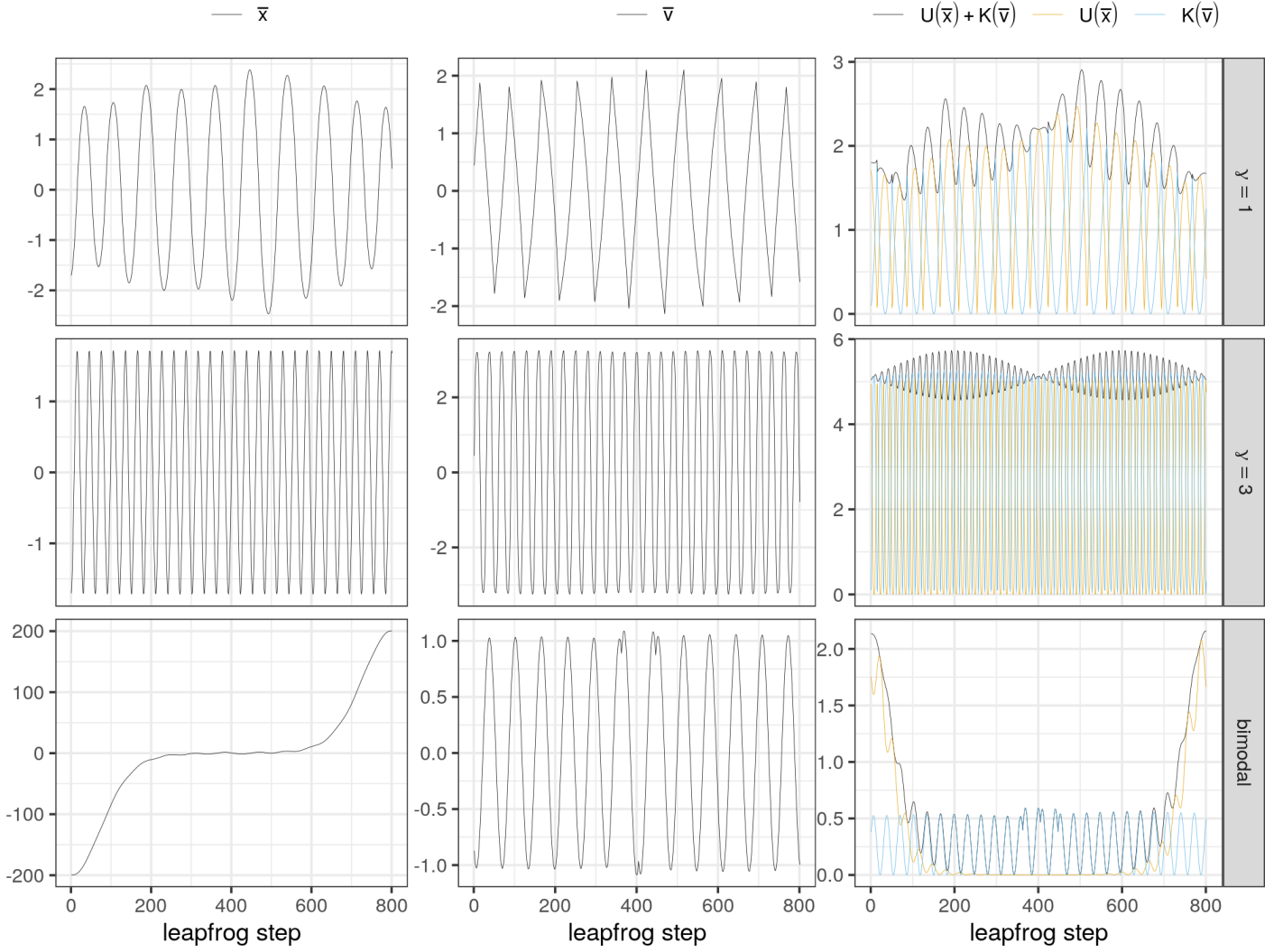


Figure 3: Traceplots for  $\bar{x} = x \cdot e^{-\frac{2}{\gamma+2}\eta}$ ,  $\bar{v} = \tilde{v} \cdot e^{\frac{2}{\gamma+2}\eta}$ , and  $U(\bar{x}) + K(\bar{v})$  for simulated paths. The potential energy functions were given by  $U(x) = |x|$  (top),  $U(x) = |x|^3$  (middle), and  $U(x) = \frac{1}{2}\phi(x; -200, 1^2) + \frac{1}{2}\phi(x; 200, 1^2)$  (bottom,  $\gamma = 2$ ). All paths were simulated with  $\eta_k = 6\{1 - \cos(2\pi k/800)\}$  and  $\tilde{\epsilon} = 0.1 \cdot \exp\{\frac{4}{\gamma+2}\eta\}$ .

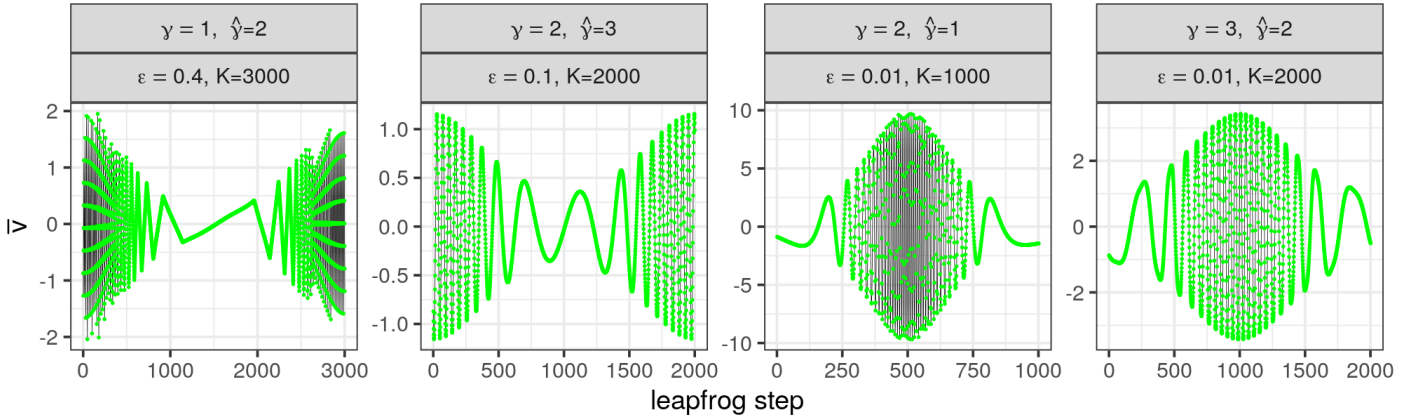


Figure 4: Traceplots for  $\bar{v} = \tilde{v} \cdot \exp\{\frac{2}{\gamma+2}\eta\}$  for simulated paths using  $\eta_k = 6\{1 - \cos(2\pi k/K)\}$  and  $\tilde{\epsilon} = \epsilon \cdot \exp\{\frac{4}{\gamma+2}\eta\}$ . The potential energy functions were given by  $U(x) = |x|^\gamma$ , where  $\gamma \neq \hat{\gamma}$ . The choices for  $K$  and  $\epsilon$  were made following the guidelines given in Section 3.3.2.

Corollary 1 implies that when  $U(x) \propto \|x\|_B^2$ , the traceplots of  $\bar{x}(t)$  and  $\bar{v}(t)$  are oscillatory with constant amplitudes and frequencies. This, on the other hand, means that both  $x = \bar{x} \cdot e^{a\eta}$  and  $\tilde{v} = \bar{v} \cdot e^{-a\eta}$  scale exponentially with varying  $\eta$ . When  $U(x) \propto \|x\|^\gamma$  with  $\gamma \neq 2$ , the equations (28) become nonlinear, and the solutions are not readily understood analytically. However, the behavior of the numerical solutions for  $(\bar{x}, \bar{v})$  when  $\gamma \neq 2$  is similar to the case for  $\gamma = 2$ , as shown in Figure 3. The numerical simulations in Figure 3 were carried out for  $(x(\tilde{t}), \tilde{v}(\tilde{t}))$  using the leapfrog method with step size  $\tilde{\epsilon} = \epsilon \cdot e^{2a\eta}$ , and then the transformation (26) was applied. The bottom row of Figure 3 further shows that  $\bar{v}(t)$  is close to sinusoidal when  $U(x)$  is the potential function of a bimodal distribution. Due to the bimodality, however,  $\bar{x}(t)$  is not sinusoidal in this case. In practical situations when  $\gamma$  is unknown, its approximate value can be estimated by finding a value  $\hat{\gamma}$  that makes  $\bar{v} := \tilde{v}e^{a\eta}$  close to sinusoidal where  $a := \hat{\gamma}/(\hat{\gamma} + 2)$ .

The following proposition will be used to show that the acceptance probability of the proposed candidate at the end of one cycle of  $\eta(t)$  is close to one.

**Proposition 3.** *Suppose that  $U(x) = c\|x\|_B^\gamma$  for some  $c, \gamma > 0$ . Then, denoting  $K(\bar{v}) = \frac{1}{2}\bar{v}^\top M\bar{v}$ , we have*

$$U\{\bar{x}(t)\} + K\{\bar{v}(t)\} - U\{\bar{x}(0)\} - K\{\bar{v}(0)\} = \int_0^t [-\gamma U\{\bar{x}(s)\} + 2K\{\bar{v}(s)\}] \cdot a \, d\eta(s).$$

*Proof.* The change in  $U(\bar{x}) + K(\bar{v})$  is described by the equation

$$\begin{aligned} \frac{d}{dt}\{U(\bar{x}) + K(\bar{v})\} &= \nabla U(\bar{x}) \cdot \frac{d\bar{x}}{dt} + \bar{v}^\top M \frac{d\bar{v}}{dt} \\ &= \nabla U(\bar{x}) \cdot \left( \bar{v} - \bar{x} \cdot a \frac{d\eta}{dt} \right) + \bar{v}^\top M \left( -M^{-1} \nabla U(\bar{x}) + \bar{v} \cdot a \frac{d\eta}{dt} \right) \\ &= \{-\nabla U(\bar{x}) \cdot \bar{x} + 2K(\bar{v})\} \cdot a \frac{d\eta}{dt} \\ &= \{-\gamma U(\bar{x}) + 2K(\bar{v})\} \cdot a \frac{d\eta}{dt} \end{aligned}$$

where we have used Proposition 2 to obtain the second equality.  $\square$

For  $a = \frac{2}{\gamma+2}$  and  $U(x) = c\|x\|_B^\gamma$  for some  $c > 0$ , we have

$$\begin{aligned} K(\bar{v}) &:= \frac{1}{2}\bar{v}^\top M\bar{v} = e^{2a\eta} \frac{1}{2}\tilde{v}^\top M\tilde{v} = e^{-\gamma a\eta} \cdot \frac{1}{2}\tilde{v}^\top (e^{2\eta} M)\tilde{v}, \\ U(\bar{x}) &= c\|\bar{x}\|_B^\gamma = e^{-\gamma a\eta} c\|x\|_B^\gamma = e^{-\gamma a\eta} \cdot U(x). \end{aligned} \tag{30}$$

If a Hamiltonian path was simulated for a full cycle of the mass scaling schedule  $\{\eta_k\}$  so that the value of  $k$  is equal to zero both at the beginning and at the end, the increment in the Hamiltonian will be given by

$$\begin{aligned} \Delta H &= \Delta U(x) + \Delta \left\{ \frac{1}{2}\tilde{v}^\top e^{2\eta_k} M\tilde{v} \right\} - \Delta \log \psi_K(k) - \Delta \left\{ \frac{1}{2} \log \det(e^{2\eta_k} M) \right\} \\ &= e^{\gamma a\eta_{k_0}} \{\Delta U(\bar{x}) + \Delta K(\bar{v})\} \\ &\approx \int_0^{K\epsilon/2} [-\gamma U\{\bar{x}(s)\} + 2K\{\bar{v}(s)\}] \cdot a \, d\eta(s) + \int_{K\epsilon/2}^{K\epsilon} [-\gamma U\{\bar{x}(s)\} + 2K\{\bar{v}(s)\}] \cdot a \, d\eta(s). \end{aligned} \tag{31}$$

Since the traceplots for  $\bar{x}(t)$  and  $\bar{v}(t)$  are oscillatory with almost constant order of magnitude, if there are enough numbers of oscillation cycles in both the first and second halves of the trajectory (say two or more in each half), the first integral in the last line of (31) can be almost exactly canceled by the second integral, because  $\eta(\frac{K\epsilon}{2}) - \eta(0) = -(\eta(K\epsilon) - \eta(\frac{K\epsilon}{2}))$ . Thus, we have

$$\Delta H \approx 0,$$

and the acceptance probability of the proposed candidate, given by  $\min(e^{-\Delta H}, 1)$ , is close to unity. We note that the number of oscillations of  $(\bar{x}(t), \bar{v}(t))$  in one cycle of  $\eta(t)$  can be readily increased by increasing the period of  $\eta(t)$ , which is equal to  $K\epsilon$ .

Parameter	Description	Tuning guidelines
$\{\eta_k\}$	mass scaling schedule	must be periodic and symmetric about zero.
$\eta_*$	amplitude of $\{\eta_k\}$	large enough to facilitate frequent mode hopping.
$K$	period of $\{\eta_k\}$	large enough that one cycle of $\{\eta_k\}$ include at least several ( $\gtrsim 5$ ) oscillation cycles of $\bar{v} = \tilde{v}e^{a\eta}$ .
$\psi_K(k)$	target distribution for $k$	$\psi_K(k) \propto \mathbf{1}[\eta_k \leq c]$ for some $c$ .
$a$	time scale coefficient	can be tuned such that both the oscillation amplitude and frequency of $\bar{v}(t) = \tilde{v}e^{a\eta}$ are almost constant. For $U(x) \propto  x ^\gamma$ , the optimal value is $a = \frac{2}{\gamma+2}$ .
$\tilde{\epsilon}$	leapfrog step size	$\tilde{\epsilon} = \epsilon \cdot e^{2a\eta}$ .
$\epsilon$	baseline leapfrog step size	small enough that each oscillation cycle of $\bar{v}$ consists of at least several ( $\gtrsim 10$ ) leapfrog steps.
$L$	number of acceptable proposals to be found in an iteration step	large enough so that the proposed candidate is not too close to the starting point.
$N$	maximum number of candidate proposals in an iteration step	large enough so that the simulated path can reach a new mode, while ensuring that the algorithm is not excessively slowed down in case unfavorable values of $v(0)$ and $\Lambda$ are drawn.

Table 1: Tuning guidelines for parameters in Algorithm 1

### 3.3.2 Tuning strategies in practice

For the mass scaling schedule given by (27), the simulated paths depend on the amplitude  $\eta_*$  but not on the additive constant  $c_\eta$ . When the mass scaling schedule  $\eta(t)$  is replaced by  $\eta'(t) = \eta(t) + c$  for some constant  $c$ , if we change  $\epsilon$  to  $\epsilon' = \epsilon \cdot e^{(-2a+1)c}$ , then the LF step size changes from  $\tilde{\epsilon} = \epsilon \cdot e^{2a\eta}$  to

$$\tilde{\epsilon}' = \epsilon' \cdot e^{2a\eta'} = (\epsilon \cdot e^{(-2a+1)c}) \cdot e^{2a(\eta+c)} = \tilde{\epsilon} \cdot e^c.$$

Under the shift  $\eta' = \eta + c$ , the initial velocity also changes to  $\tilde{v}'(0) = \tilde{v}(0) \cdot e^{-c}$ , since  $\tilde{v}(0) \sim \mathcal{N}(0, e^{-2\eta} M^{-1})$ . Thus we have  $\tilde{v}' \cdot \tilde{\epsilon}' = \tilde{v} \cdot \tilde{\epsilon}$ , and the displacement in  $x$  made by each leapfrog step is unchanged. This means that the numerical simulation by the leapfrog method gives the same result when  $\eta(t)$  is shifted by a constant. In what follows, we will assume that the minimum value of  $\eta(t)$  is equal to zero without loss of generality.

The maximum amount of increase in  $\eta(t)$ , which is equal to  $2\eta_*$  for (27), affects how far the simulated Hamiltonian paths reach when isolated modes are searched for. Since  $\bar{x}$  and thus  $U(\bar{x})$  are of approximately constant order of magnitude for a simulated path, due to the relationship  $U(x) = e^{\gamma a \eta} U(\bar{x})$  shown in (30), the increase in the potential energy  $U(x)$  scales approximately linearly with  $e^{\gamma a \eta}$ . The typical height of a potential barrier for a given  $U(x)$  can be approximately estimated by the difference in  $U(x)$  evaluated at a local minimum and at an arbitrary point in the suitable region of the target space where isolated modes are expected to be found. Thus the amplitude of  $\eta(t)$  can be then chosen such that

$$\gamma a \cdot 2\eta_* = \frac{4\gamma}{\gamma+2} \eta_* \gtrsim \log(\text{the height of potential energy barriers}).$$

Since the maximum increase in  $\eta(t)$  along a simulated path relative its starting value determines the search scope, it is beneficial to start the path at the smallest values of  $\eta(t)$ . Thus, the distribution on  $k$  of the form

$$\psi_K(k) = \frac{\mathbf{1}[\eta_k \leq c]}{\sum_{k'=1}^K \mathbf{1}[\eta_{k'} \leq c]} \quad \text{for some } c$$

can lead to a higher mode hopping frequency. This choice has an additional advantage that it can reduce the number of Hamiltonian evaluations. The Hamiltonian  $H(Y_n, k_0 + n, W_n)$  is evaluated

in line 13 of Algorithm 1 to check if a proposed candidate is acceptable. The evaluation of the Hamiltonian is only necessary for  $k_0+n$  in the support of  $\psi_K$ , because otherwise the  $-\log \psi_K(k_0+n)$  term in the Hamiltonian function is equal to infinity.

In practical applications, the polynomial degree  $\gamma$  with which  $U(x)$  increases may be unknown, and the value for the time scale coefficient  $a$  may need to be determined. To do this, one may first run an MCMC algorithm such as HMC for a few iterations until the constructed chain reaches a local basin of  $U(x)$ . Starting from a point in that local basin, one may then simulate a path with slowly varying  $\eta$  and an initial choice for  $a$ , and plot  $\bar{v}(t) = \tilde{v} \cdot e^{a\eta}$  as a function of  $t$ . If the oscillation amplitude of  $\bar{v}(t)$  decreases with increasing  $\eta$ , the value of  $a$  should be increased, and in the opposite case, it should be decreased. This step should be repeated a few times until  $\bar{v}(t) = \tilde{v}e^{a\eta}$  has an approximately constant oscillation amplitude.

In order to have a high acceptance probability for a proposed candidate, we should have  $\Delta H \approx 0$  at the end of a full cycle of  $\eta(t)$ . For this, the first and the second integrals in (31) should almost cancel each other. This may not happen if there is only a fraction of an oscillation cycle for  $\bar{v}(t)$  in each half of the simulated path. Therefore, it is advisable that the path is simulated for a sufficient amount of time, which can be achieved by letting

$$K\epsilon\rho \gtrsim 5 \quad (32)$$

where  $\rho$  signifies the frequency of the oscillations of  $\bar{v}(t)$ . On the other hand, in order for the numerical simulation of  $(x(\tilde{t}), \tilde{v}(\tilde{t}))$  to be stable and accurate, the LF step size should be sufficiently small so that each cycle of oscillation of  $\bar{v}(t)$  consists of at least a few leapfrog steps. To ensure this we can let

$$\epsilon\rho \lesssim \frac{1}{10}. \quad (33)$$

Algorithm 1 is moderately robust with respect to incorrect estimation of  $\gamma$ . Suppose that a Hamiltonian path is simulated with  $\tilde{\epsilon} = \epsilon \cdot e^{2a\eta}$  where  $a = \frac{2}{\hat{\gamma}+2}$  and  $\hat{\gamma} \neq \gamma$ . If  $\hat{\gamma} < \gamma$  and  $a > \frac{2}{\gamma+2}$ , since  $d\tilde{t} = dt \cdot e^{2a\eta}$ , the path is simulated for a longer amount of time in the interval where  $\eta$  is large than when the optimal choice of  $a$  is used. The opposite is true if  $\hat{\gamma} > \gamma$  and  $a < \frac{2}{\gamma+2}$ .

Figure 4 shows the traceplots for  $\bar{v} = \tilde{v} \cdot e^{\frac{2}{\hat{\gamma}+2}\eta}$  as a function of the number of leapfrog steps when  $\gamma$  is misspecified. For instance, when  $\gamma = 3$ ,  $\hat{\gamma} = 2$ , and  $\max_t \eta(t) = 2\eta_* = 12$ , the speed of time advancement in  $\tilde{t}$  is increased by a factor of  $e^{2(a-\frac{2}{\gamma+2})\eta(t)} = e^{2(\frac{2}{\hat{\gamma}+2}-\frac{2}{\gamma+2}) \cdot 12} \approx 11$  when  $\eta(t)$  is at its maximum. Thus  $\bar{v}(t)$  oscillates approximately eleven times faster at the maximum of  $\eta(t)$  than when  $\eta(t) = 0$ . The condition (33) can still be satisfied if  $\epsilon$  is decreased by a factor of eleven. In summary, when  $\gamma$  is incorrectly estimated, the desired result  $\Delta H \approx 0$  can be achieved by ensuring that (32) is satisfied when the oscillation frequency  $\rho$  is smallest and that (33) is satisfied for when  $\rho$  is greatest.

**Example 3.2** Suppose that the target density is given by

$$\pi(x) = \frac{1}{2}\phi(x; \mu_1, I) + \frac{1}{2}\phi(x; \mu_2, I), \quad x \in \mathbf{R}^{10000},$$

where  $\|\mu_1 - \mu_2\|_2 = 400$  and each mixture component has the identity covariance matrix. The left plot in Figure 5 shows an example trajectory constructed by numerically solving (18) using the leapfrog method (23) where the mass scaling schedule is given by  $\eta_k = 6\{1 - \cos(2\pi k/1500)\}$  and the LF step sizes are given by  $\tilde{\epsilon} = 0.1 \cdot \exp\{\frac{4}{\gamma+2}\eta\}$  with  $\gamma = 2$ . The path slowly spirals out of the initial mode as the total energy increases due to increasing mass. Near the maximum of  $\eta$  the path searches the 10000 dimensional space using the gradient information of the potential energy function. As the mass decreases during the second half, the path spirals down to a different mode. The increment in the Hamiltonian at the end of this trajectory is 0.68.

The right plot in Figure 5 shows a constructed Markov chain of length one hundred. The distribution  $\psi_K(k) \propto 1[|k| \leq 4]$  was used. Among the one hundred iteration steps, there were seventy one accepted moves, and among them thirty five were jumps between the two modes.  $\square$

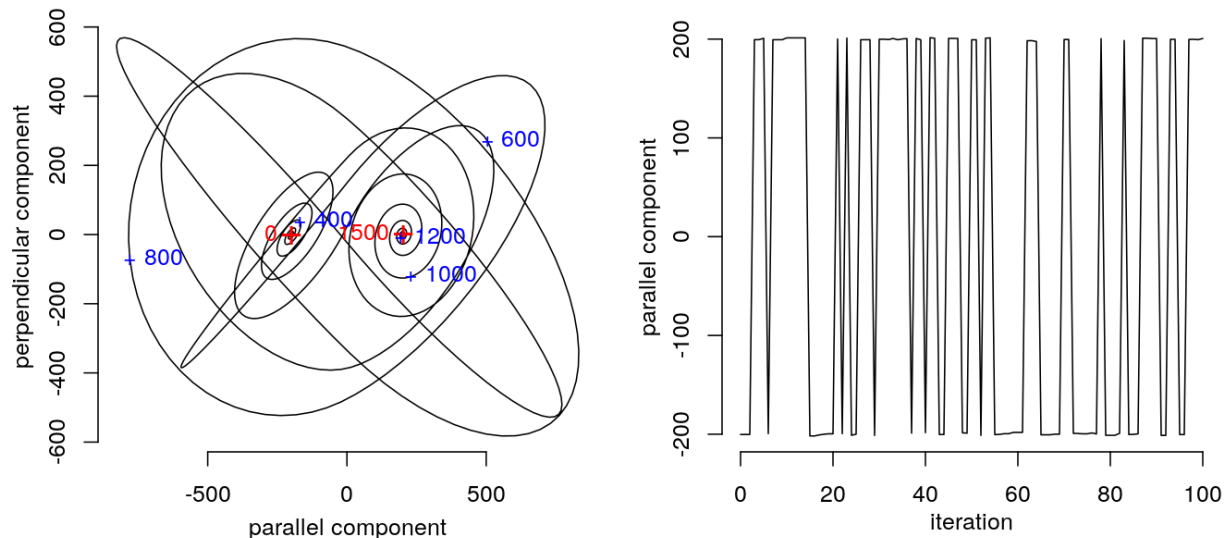


Figure 5: Left; an example of simulated Hamiltonian paths for  $d = 10,000$  dimensional target distribution considered in Example 3.2. The  $x$ -axis shows the projection to the direction parallel to the vector  $\mu_2 - \mu_1$ , and the  $y$ -axis shows the projection to a direction perpendicular to  $\mu_2 - \mu_1$ . The initial and the terminal points are marked by red + signs, and a few selected intermediate points by blue + signs. The numbers on the plot indicate the leapfrog step number. Right; a draw of Markov chain obtained by running Algorithm 1, projected to the direction parallel to  $\mu_2 - \mu_1$ .

We note that the acceptance probabilities in practical applications can be smaller than as illustrated in Example 3.2. The phenomenon of low acceptance probability can occur due to the fact that the target distribution may have complex potential energy landscape. The simulated path is more likely to settle in a local basin that occupies a large volume in the target space, but that local basin may occupy a small probability of the target distribution. If this is the case, the proposed candidate in that basin should be rejected with a high probability, since the target distribution should be invariant under stationarity. This issue was discussed in Section 5 of Neal (1996).

## 4 Applications

### 4.1 Self-localization of a sensor network

We test Algorithm 1 on a sensor network self-localization problem considered by Ihler et al. (2005). The goal in this example is to find the locations of sensors in a two dimensional region using noisy pairwise distance measurements. There are eight sensors (labeled 1–8) at unknown locations and three sensors (labeled 9–11) at known locations. The sensors with known locations serve to remove or reduce unidentifiability due to translation, rotation, and mirror symmetry. All sensors are located in the unit square  $[0, 1]^2$ . The distance between each pair of sensors is measured with probability given by  $e^{-\|x_t - x_u\|^2 / (2R^2)}$  where  $x_t$  and  $x_u$  denote the locations of the sensors and  $R = 0.3$ . If the distance is measured, the measurement follows the distribution  $\mathcal{N}(\|x_t - x_u\|, \sigma_e^2)$  where  $\sigma_e = 0.02$ . We used the independent, uniform prior on the unit square for the unknown sensor locations. For data generation, the eleven sensor locations were randomly selected in the unit square. The distance measurement data were generated using the assumed measurement model. The posterior density for  $x_{1:8}$  given the data was a function of only the pairwise distances between the sensors  $x_{1:11}$ , except for the constraint term that bounds the location of each sensor to the unit square. Two of the three sensors of known locations ( $x_9$  and  $x_{10}$ ) happened to be close to each other (see Figure 6). Thus the unknown locations of the sensors  $x_{1:8}$  were not strongly



identifiable with respect to the mirror symmetry about the line that approximately connected the known sensor locations  $x_{9:11}$ . This led to strong bimodality in the posterior distribution for  $x_{1:8}$ , since the generated sensor locations and its mirror image about the symmetry line had almost equal likelihoods.

We constructed twelve independent Markov chains in parallel targeting the posterior distribution of the unknown sensor locations  $x_{1:8}$  using tempered Hamiltonian transitions (Algorithm 1). The initial states of the sensor locations were randomly drawn in the unit square. All parallel chains were constructed until they had one thousand sampled states. The top six panels in Figure 6 show the marginal distributions of the posterior draws for the eight unknown sensor locations from six of the twelve parallel chains. The mass scaling schedule  $\eta_k = \eta_* \{1 - \cos(2\pi k/K)\}$  and leapfrog step sizes  $\tilde{\epsilon} = \epsilon \cdot \exp\{\frac{4}{\hat{\gamma}+2}\eta\}$  were used, where  $\eta_* = 2$ ,  $K = 2000$ ,  $\epsilon = 0.001$ , and  $\hat{\gamma} = 2$ . These tuning parameters were selected by using simulated pilot paths starting from the states reached by running standard HMC for a short time. The maximum mass scaling factor of  $e^{2\cdot 2\eta_*} = e^8$  was large enough to enable global moves between local modes, and  $K = 2000$  and  $\epsilon = 0.001$  were chosen such that the increment in the Hamiltonian is close to zero at the end of the simulated paths. The value of  $\hat{\gamma} = 2$  was chosen to ensure that  $\bar{v}$  has approximately constant amplitude and frequency. The distribution  $\psi_K(k)$  was chosen to be uniform on the support  $\{k; |k| \leq 30\}$ . Each iteration step continued until either  $L = 20$  acceptable candidates were found or  $N = 2200$  leapfrog steps were carried out. The Hamiltonian paths were simulated with reflection at the boundaries by negating the components of the velocity variable that fell outside the interval  $[0, 1]$ , since all sensors were located inside the unit square.

All twelve parallel Markov chains constructed by Algorithm 1 identified both modes of the posterior distribution. Figure 6 only shows the first six of the twelve chains. The marginal distributions of the sampled sensor locations were symmetric about the red dashed line connecting the sensors of known locations. One of the two sampled posterior modes closely matched the generated locations of the sensors. We note that the sensor labeled 2 had no distance measurements with any other sensors, so its marginal posterior distribution was almost evenly spread out in the regions where no sensors were close by. For comparison with these results, we constructed twelve parallel Markov chains targeting the same posterior distribution by running Algorithm 1 with  $\eta(t)$  constant at zero, which makes the algorithm equivalent to a standard HMC. The marginal distributions of the posterior draws from six of these twelve chains are shown in the bottom half of Figure 6. Unlike the posterior draws constructed by tempered Hamiltonian transitions, each of the parallel chains constructed by standard HMC found only one local mode, and for three of the six chains shown in Figure 6 (and for six of the total twelve chains), the discovered local mode was not one of the two dominant posterior modes. The posterior densities at these non-dominant modes were about  $e^5$ – $e^{10}$  times smaller than those at the two dominant modes. There occurred no transitions between local modes in any of the twelve parallel chains constructed by standard HMC (Supplementary figure S-6).

Figure 7 shows the joint pairwise posterior distributions for the  $y$ -coordinates of the sensors for one of the twelve Markov chains constructed using tempered Hamiltonian transitions ( $\eta_* = 2$ ). This figure clearly displays the multimodality in joint posterior distribution. The pairplots for the other eleven constructed chains showed the same modes (figures not shown). Figure 8 shows that the constructed chain jumped between the two dominant posterior modes after it reached stationarity. After discarding the first thirty iterations as burn-in from each constructed Markov chain, there occurred an average of 12.5 mode hops in the remaining 970 iteration steps for the twelve chains. The standard deviation of the number of mode hops was 4.3. We also ran the algorithm with different values of  $\eta_*$  at 2.5 and 3, and the numerical results were almost the same as those shown in Figure 6–8 (see the supplementary figures in Section S3.2 and S3.3). These results imply that Algorithm 1 is reasonably robust with respect to the tuning of the maximum mass scale factor, provided that it is large enough to enable mode hops.

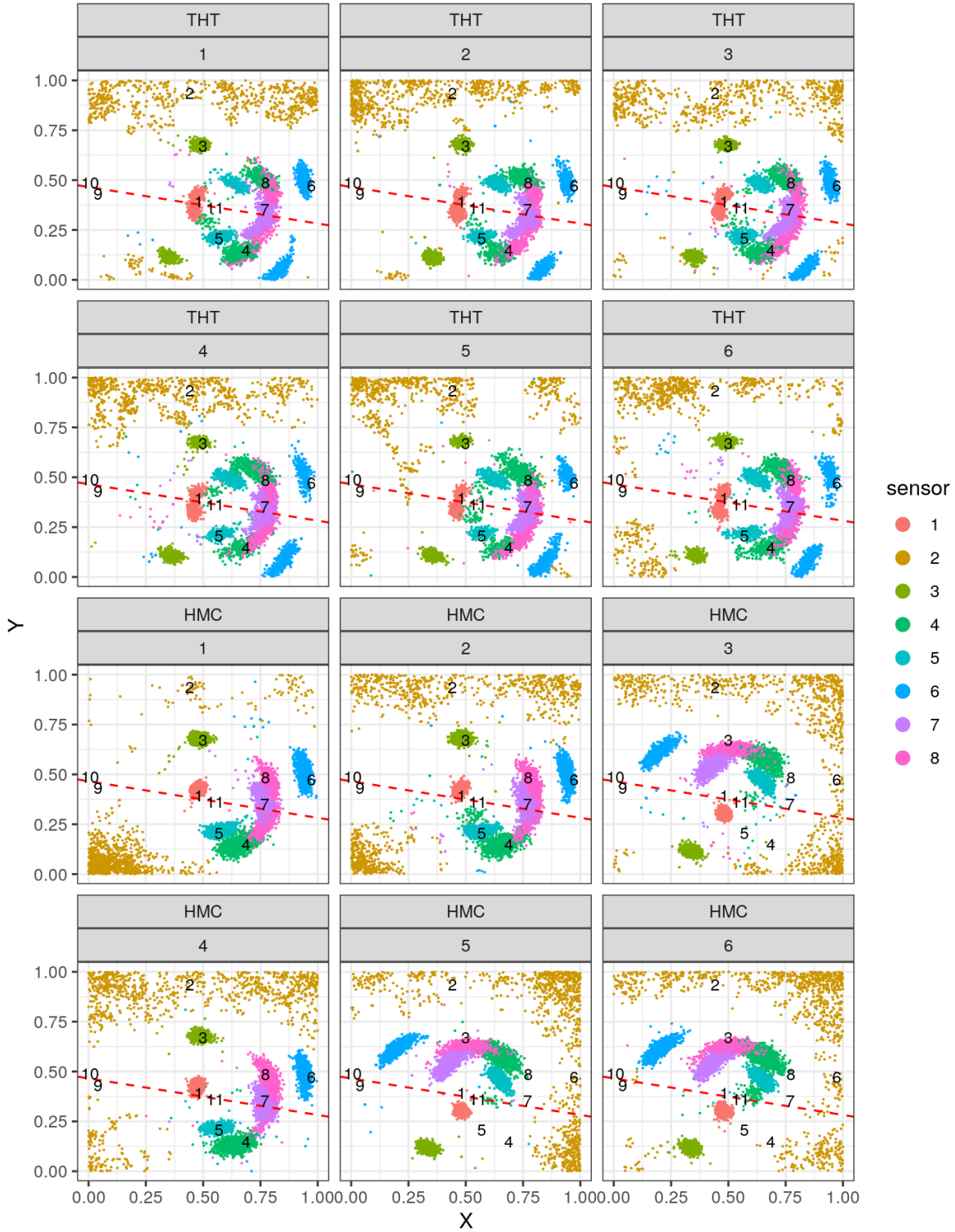


Figure 6: The marginal distributions of the posterior draws for the unknown sensor locations from six independently constructed Markov chains using tempered Hamiltonian transitions (THT, Algorithm 1) and from six chains constructed using standard HMC. The true location of each sensor is marked on the plot by its number label. The locations of sensors 9, 10, and 11 were known. The two dominant posterior sensor configurations were mirror-symmetric about the red dashed line connecting the known sensor locations. The parameters  $R = 0.3$  and  $\sigma_e = 0.02$  were assumed to be known.



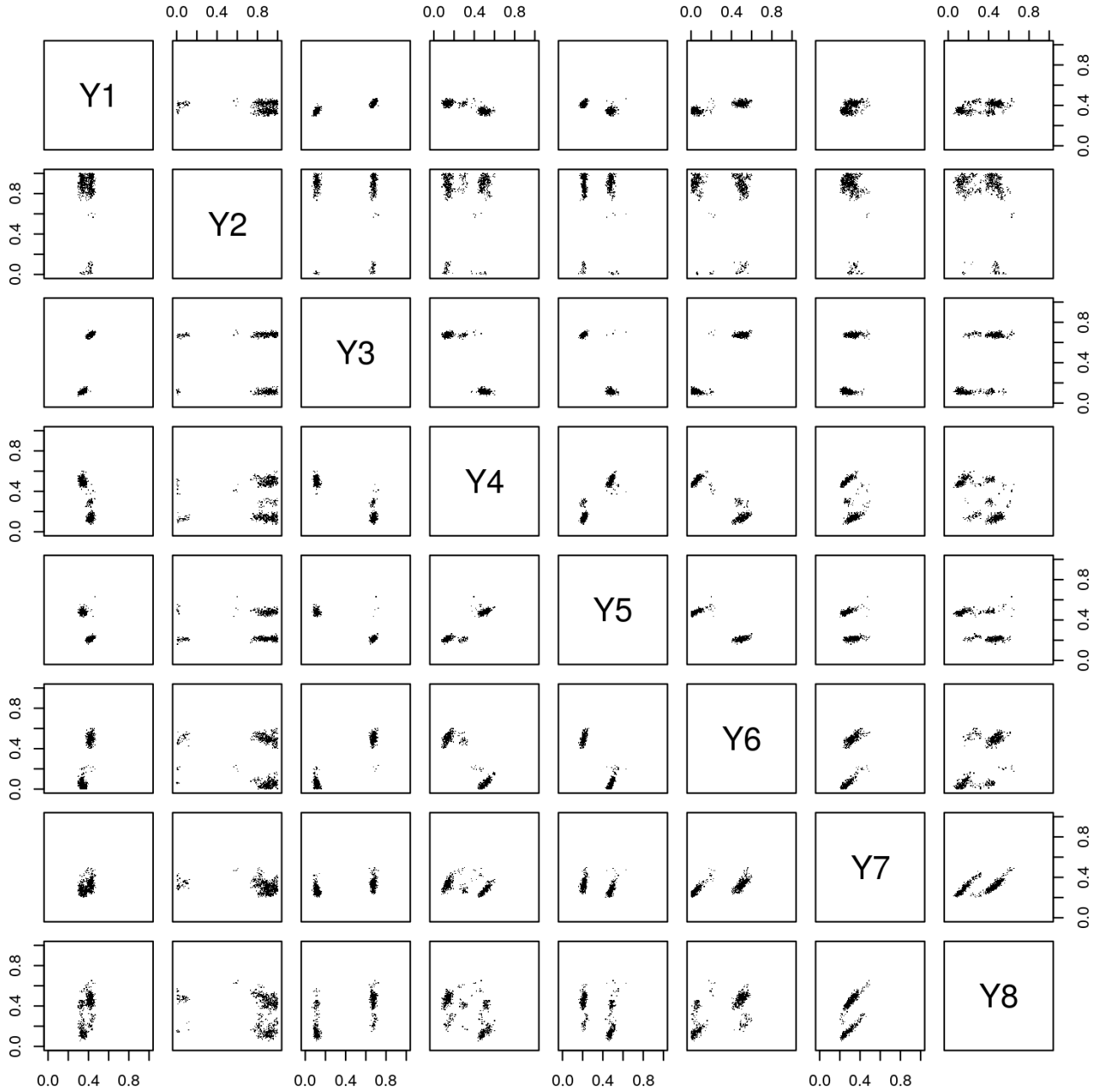


Figure 7: Pairwise distributions of the posterior draws for the  $y$ -coordinates of the sensor locations from one of the Markov chains constructed using Algorithm 1. The joint bimodality is clearly shown. The parameters  $R = 0.3$  and  $\sigma_e = 0.02$  were assumed to be known.

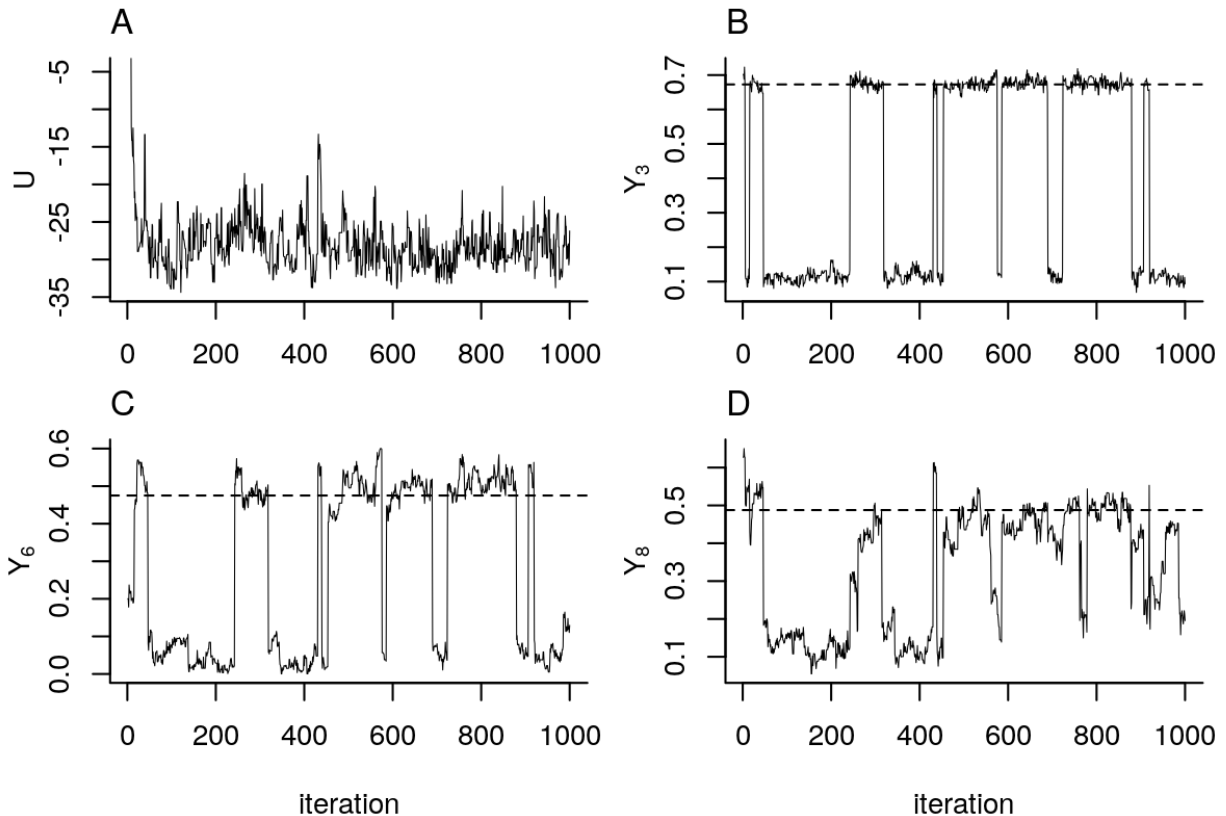


Figure 8: The traceplot of the potential energy  $U(\mathbf{x}_{1:8}) = -\log \pi(\mathbf{x}_{1:8}|\text{data})$  and the  $y$ -coordinates of the third, sixth, and eighth sensors for one of the twelve Markov chains constructed in parallel using tempered Hamiltonian transitions (Algorithm 1). The true  $y$ -coordinates are shown by the dashed horizontal lines. The parameters  $R = 0.3$  and  $\sigma_e = 0.02$  were assumed to be known.

## 4.2 Self-localization of a sensor network for unknown $R^2$ and $\sigma_e^2$

As briefly mentioned in Section 1, simulated tempering and parallel tempering may not be readily implemented in the Gibbs sampler settings, because the former requires the mixture weights to be tuned for each new conditional distribution and the latter requires a burn-in period for the parallel chains targeting different tempered distributions. Here we demonstrate tempered Hamiltonian transitions within a Gibbs sampler using the sensor network self-localization problem. For this, we considered the parameters  $R$  and  $\sigma_e$  to be unknown. We ran the Gibbs sampler by alternating between the step where the sensor locations  $\mathbf{x} := \mathbf{x}_{1:8}$  were drawn conditional on  $R$  and  $\sigma_e$  and the step where  $R$  and  $\sigma_e$  were drawn conditional on  $\mathbf{x}$ . We used the exponential distributions with rate  $1/0.5$  and  $1/0.05$  for the prior distributions for  $R$  and  $\sigma_e$ . The values of  $R$  and  $\sigma_e$  were drawn on the log scale given  $\mathbf{x}$  to remove the positivity constraints. In this model,  $R$  and  $\sigma_e$  were conditionally independent given  $\mathbf{x}$ , so we drew these two parameters separately, using standard HMC where each iteration step made thirty leapfrog steps of size 0.02. We used tempered Hamiltonian transitions (Algorithm 1) for drawing  $\mathbf{x}$  given  $R$  and  $\sigma_e$ . We used the same dataset used in Section 4.1, as well as the same  $\{\eta_k\}$ ,  $\tilde{\epsilon}$ , and  $\psi_K$ .

We independently constructed twelve Markov chains targeting the joint posterior distribution for  $\mathbf{x}$ ,  $R$ , and  $\sigma_e$  using the Gibbs sampler. Figure 9 shows the traceplots of various quantities from one of the twelve constructed chains. The traceplots for the potential energy,  $U(\mathbf{x}) = -\log \pi(\mathbf{x}|R, \sigma_e, \text{data})$ , and the combined log posterior density,  $\log \pi(\mathbf{x}, R, \sigma_e|\text{data})$ , suggest that the chain reached stationarity. The posterior draws for  $R$  and  $\sigma_e$  were close to the values used to generate the data. The constructed chain hopped between the two dominant posterior modes for the sensor locations. Table 2 summarizes the numerical results. Algorithm 1 took 21.4 minutes

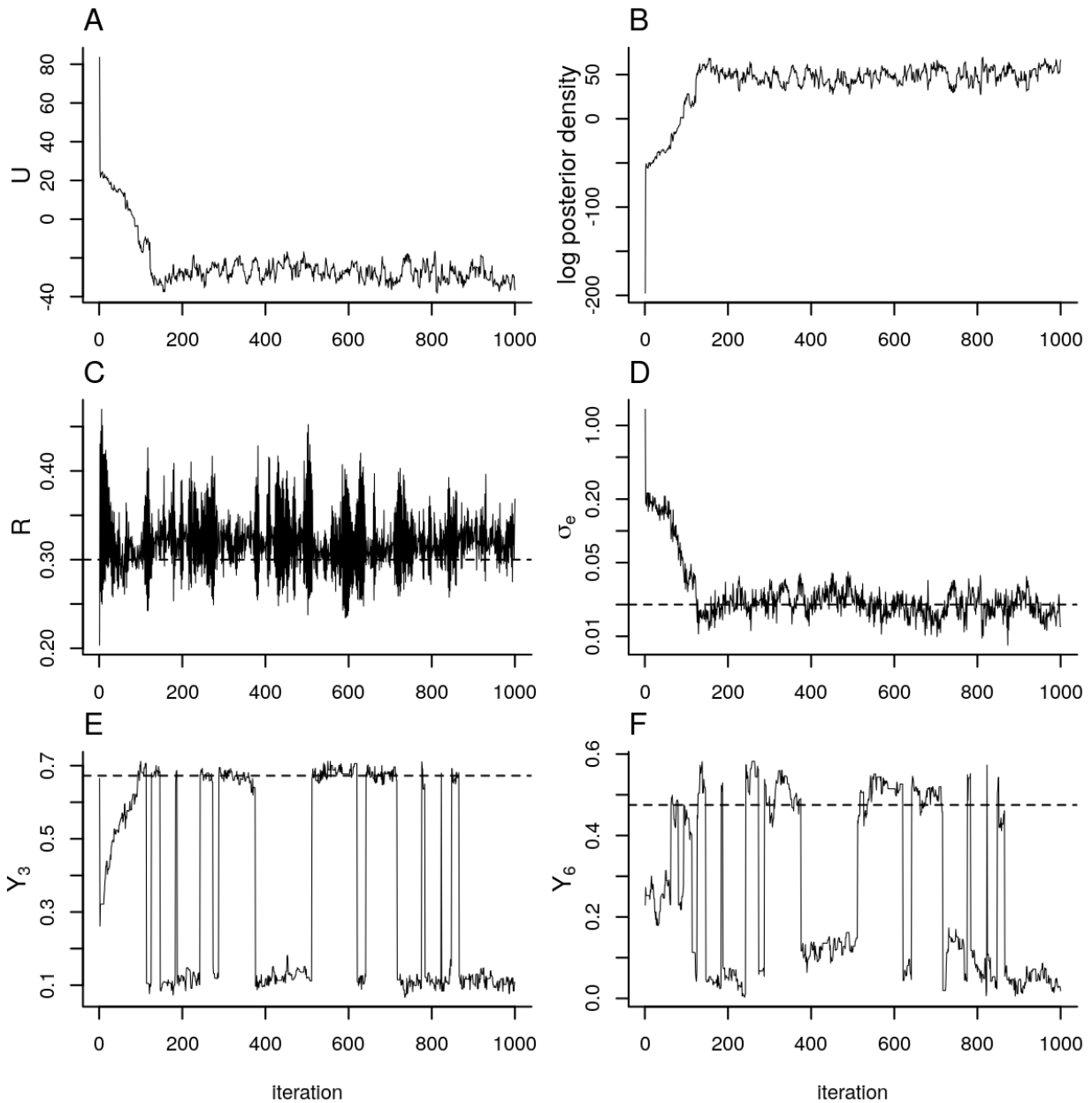


Figure 9: The traceplots of various quantities for one of the twelve parallel chains constructed by tempered Hamiltonian transitions targeting the posterior distribution of the sensor locations and the parameters  $R$  and  $\sigma_e$  (Section 4.2). A, the potential energy  $U(\mathbf{x}) = -\log \pi(\mathbf{x}|R, \sigma_e, \text{data})$ ; B, the log posterior density  $\log \pi(\mathbf{x}, R, \sigma_e|\text{data})$ ; C,  $R$ ; D,  $\sigma_e$ ; E,F, the  $y$ -coordinates of the third and the sixth sensors. The values of  $R$ ,  $\sigma_e$ , and the  $y$ -coordinates of the third and the sixth sensors used to generate the data are marked by dashed horizontal lines in C–F.

	iterations	runtime	$t_{\text{reach}}$ (s.d.)	$n_{\text{hop}}$ (s.d.)	$\hat{R}$ (min, avg, max)
THT	1000	21.4	3.6 (2.4)	8.5 (4.6)	1.01, 1.07, 1.11
HMC	35000	23.3	4.5 (4.6)	0 (0)	1.01, 1.34, 1.85

Table 2: Comparison of tempered Hamiltonian transitions (Algorithm 1) and standard HMC on the sensor localization problem where  $R$  and  $\sigma_e$  are assumed to be unknown. The table shows the number of iterated steps, runtime in minutes, average time in minutes for the chains to reach one of the two dominant posterior modes for the sensor locations ( $t_{\text{reach}}$ ) and the associated standard deviation, the average number of hops between the modes that happened after the chains reached stationarity ( $n_{\text{hop}}$ ) and the associated standard deviation, and the minimum, average, and maximum  $\hat{R}$  statistics for the eighteen target variables (namely the  $x$ ,  $y$ -coordinates of the eight unknown sensor locations,  $R$ , and  $\sigma_e$ ).

to construct twelve parallel Markov chains of length one thousand using twelve CPU cores. On average, it took 3.6 minutes for the chains to reach one of the two dominant posterior modes. Each chain was considered to have reached one of the two dominant modes if the average of the log posterior density  $\log \pi(\mathbf{x}, R, \sigma_e | \text{data})$  for the next twenty iteration steps were higher than 46.3. The chains hopped on average 8.5 times between the two dominant modes once they have reached one of the two dominant modes. We computed the potential scale reduction factor, or the  $\hat{R}$  statistic, for each of the eighteen target variables using the twelve constructed chains (Gelman et al., 2013; Gelman and Rubin, 1992). An  $\hat{R}$  statistic value close to one indicates that the between-chain variance is comparable to the within-chain variance, suggesting that the chains that started with varying initial states reached a common stationary distribution. We used the rank-normalized  $\hat{R}$  implemented in the `Rhat` function in R package `rstan` (Vehtari et al., 2019; Stan Development Team, 2020). The average of the eighteen  $\hat{R}$  statistic values was 1.07, and their maximum was 1.11 (for  $y_8$ ). Since the chains consistently hopped between the two modes, the  $\hat{R}$  values would have continued to decrease if we kept running the Gibbs sampler.

For comparison, we constructed another set of twelve parallel chains using the Gibbs sampler where standard HMC was used for drawing  $\mathbf{x}$  given  $R$  and  $\sigma_e$ . Thirty leapfrog steps of size 0.001 were made to obtain candidate proposals. Each chain was constructed for 35,000 iterated steps. This took 23.3 minutes on twelve CPU cores. All twelve chains reached one of the two dominant posterior modes for the sensor locations, but once they reached one of the two modes, they did not hop from one mode to another. The mean and the maximum  $\hat{R}$  statistic values for the eighteen target variables were 1.34 and 1.85 respectively, where the maximum  $\hat{R}$  was attained for  $Y_6$ . These  $\hat{R}$  value would have hardly decreased even if we constructed longer chains, since the chains did not jump between the modes.

We remark that Algorithm 1 can be tuned in a way that works simultaneously for various conditional distributions targeted at different iteration steps in the Gibbs sampler. As mentioned at the end of Section 4.1, if a certain value of  $\eta_*$  enabled reasonably frequent hops between the posterior modes, higher values of  $\eta_*$  would also enable the hops. The value of  $K$  can be then chosen following the guideline in Table 1. Therefore in practice, frequent hops between modes can be facilitated for various conditional distributions by using reasonably large values of  $\eta_*$  and  $K$ .

## 5 Auxiliary strategy when the support is disconnected

When the support of the target density  $\text{supp}(\pi) := \{x \in \mathbb{X}; \pi(x) > 0\}$  is disconnected, the Hamiltonian path started from one density component cannot reach other disconnected components. This issue comes from the fact that the potential energy  $U(x) = -\log \pi(x)$  is infinite on  $\text{supp}(\pi)^c = \{x; \pi(x) = 0\}$ . In this section, we consider an auxiliary strategy for Algorithm 1 that enables jumps between disconnected density components. We consider addition of a small mixture

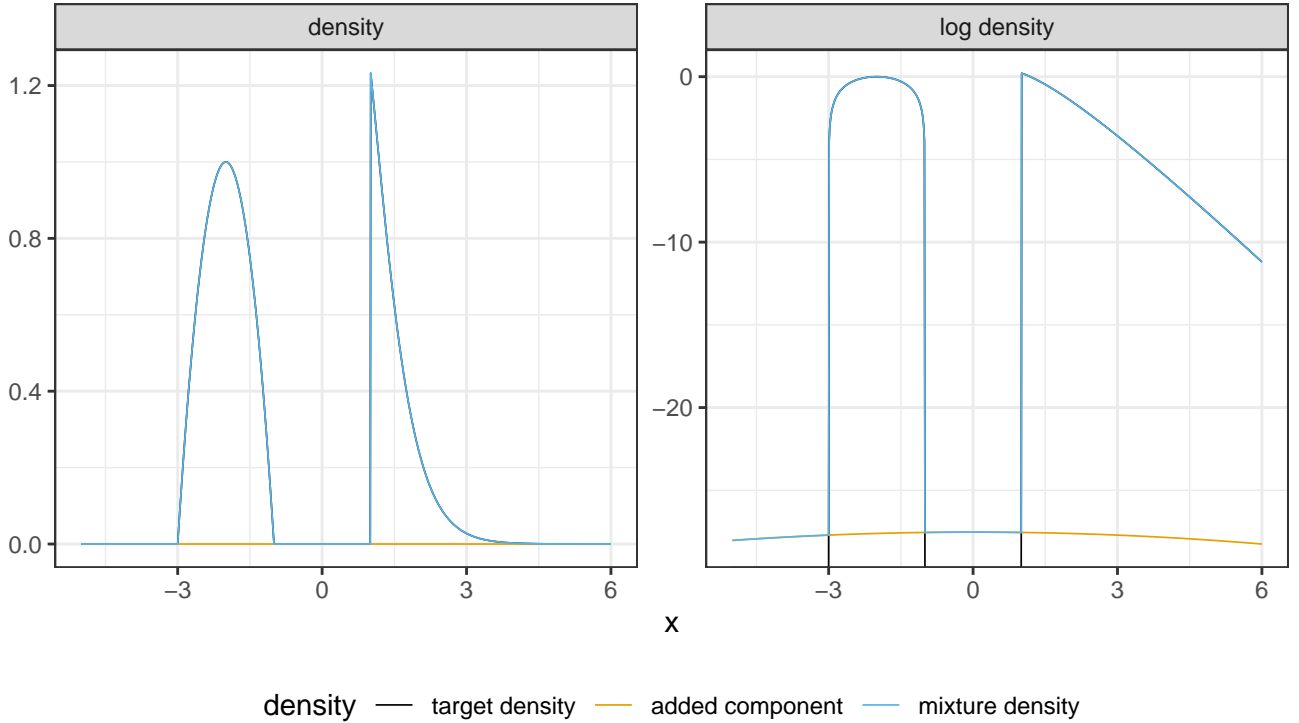


Figure 10: An illustrative diagram showing the effect of adding a small mixture component. The target density  $\pi(x)$  and the mixture density  $\pi^+(x)$  are visually indistinguishable on the natural (non-log) scale, because the weight of the added mixture component  $\nu = e^{-25}$  is tiny. However,  $\log\{\pi^+(x)\}$  is lower bounded by  $\log\{\nu g(x)\}$ , so finite everywhere.

component to the target distribution, so that the MCMC algorithm instead targets

$$\pi^+(x) = \pi(x) + \nu g(x).$$

Here  $\pi(x) = Z\bar{\pi}(x)$  is an unnormalized target density function,  $\nu$  a small positive constant, and  $g(x)$  the probability density of the added mixture component. We assume that  $g(x)$  can be evaluated pointwise. This mixture component is intended to bridge separated density components. Figure 10 shows  $\pi(x)$ ,  $\nu g(x)$ , and the sum  $\pi^+(x)$  where

$$\begin{aligned} \text{supp}(\pi) &= (-3, -1) \cup (1, \infty), \\ \pi^+(x) &= \pi(x) + e^{-25}\phi(x; 0, 5^2). \end{aligned}$$

Since  $\log \pi^+(x)$  is lower bounded by  $\log(\nu g(x))$ , Algorithm 1 targeting  $\pi^+(x)$  can construct Markov chains that jump between the two separated components of  $\text{supp}(\pi)$ . Once a sample Markov chain has been constructed by Algorithm 1 targeting  $\pi^+(x)$ , draws from the original target density  $\pi(x)$  can be obtained using rejection sampling. Provided that the states of the constructed Markov chain can be considered as draws from  $\pi^+$ , rejection sampling accepts a state  $x$  with probability

$$\frac{\pi(x)}{\pi(x) + \nu g(x)}.$$

It can be readily checked that the accepted draws can be considered as samples from the original target density:

$$\frac{\pi(x) + \nu g(x)}{Z + \nu} \cdot \frac{\pi(x)}{\pi(x) + \nu g(x)} \propto \frac{\pi(x)}{Z}.$$

In order to reduce the number of draws lost by the rejection sampling, the mixture weight  $\nu$  can be chosen such that  $\nu g(x) \ll \pi(x)$  for typical posterior draws. Section 3.3 shows that Algorithm 1

can enable jumps across a potential energy barrier whose height  $\Delta$  scales exponentially with the maximum increase in the mass scaling schedule  $\eta(t)$ . Thus for a typical posterior draw  $x_1$  from  $\pi$  and a point  $x_2 \in \text{supp}(\pi)^c$  between the disconnected components of  $\text{supp}(\pi)$ , we can choose  $\nu$  such that the difference in the potential energy, which is given by

$$\log \pi^+(x_1) - \log \pi^+(x_2) \approx \log \pi(x_1) - \log(\nu g(x_2)),$$

is on the order of  $e^{\gamma \alpha \{\max \eta(t) - \min \eta(t)\}}$  (see (30)). Therefore, the mixture weight  $\nu$  can be chosen exponentially small. For such tiny  $\nu$ , it is likely that all of the MCMC draws from  $\pi^+(x)$  survive the rejection sampling.

The mixture density  $g(x)$  should be chosen such that the graph of  $\log g(x)$  is more flat than that of  $\log \pi(x)$ , so that the disconnected components of  $\text{supp}(\pi)$  are bridged by  $g(x)$ . However, if it is excessively flat, the constructed Hamiltonian paths may unnecessarily reach far beyond the region where most of the probability mass of  $\pi(x)$  is placed. A reasonable choice in practice may be to let  $g(x)$  be the density of a normal distribution that covers most of the region where the support of  $\pi(x)$  is expected to be located.

## 6 Related work

In this section, we briefly describe some of the approaches to sampling from multimodal distributions that were developed in recent years. Continuous tempering is a strategy originally developed for, similar to various other tempering methods, simulating molecular dynamics where the free energy function has multiple isolated modes (Gobbo and Leimkuhler, 2015; Lenner and Mathias, 2016). It extends the Hamiltonian system by including a variable  $x_T \in \mathbb{R}$  linked to the temperature level and the associated velocity variable  $v_T$ . The extended Hamiltonian can be written in the form of

$$\hat{H}(x, v, x_T, v_T) = H(x, v) - f(x_T)G(x, v) + w(x_T) + \frac{1}{2}m_T v_T^2$$

where  $f$ ,  $G$  and  $w$  are some functions and  $m_T \in \mathbb{R}$  represents the mass associated with the added variable  $x_T$ . The link function  $f$  is chosen such that  $f(x_T) = 0$  for a certain interval, say for  $x_T \in (-c_T, c_T)$ . The states in the constructed Markov chain for which  $x_T \in (-c_T, c_T)$  may then be considered as draws from the original target density  $\Pi(x, v) \propto e^{-H(x, v)}$ . Graham and Storkey (2017) considered the case

$$f(x_T) = 1 - \beta(x_T), \quad G(x, v) = U(x) + \log g(x)$$

where  $\beta(x_T)$  represents the inverse temperature and  $g(x)$  is the normalized density function of a certain base distribution. In this case, the extended Hamiltonian defines a smooth transition between the target density  $e^{-U(x)}$  and  $g(x)$  such that the distribution of  $X$  given  $\beta(x_T) = \beta^*$  has density

$$p(x | \beta(x_T) = \beta^*) \propto e^{-U(x)\beta^*} g(x)^{1-\beta^*}.$$

This density function has the same form as the bridging density commonly used by annealed importance sampling (Neal, 2001). Like simulated tempering, the continuous tempering strategy becomes efficient when the temperature variable is marginally evenly distributed across its range. If the marginal distribution is highly concentrated on low temperature values, mode hopping between isolated modes may occur with extremely low probability. On the contrary, if the distribution is concentrated on high temperature values, the samples from the original target distribution may be obtained rarely. In order to achieve an even distribution of temperature, techniques such as adaptive biasing force have been used (Darve and Pohorille, 2001). Luo et al. (2019) considered continuously tempered Hamiltonian Monte Carlo using the adaptive biasing force. They further developed the method for the case where mini-batches are used, by introducing Nose-Hoover thermostats (Nosé, 1984; Hoover, 1985). The adaptive biasing technique, however, uses the history of the Markov

chain and therefore experiences the same issue of slow adaptation, which can be problematic in the Gibbs sampling settings.

Darting Monte Carlo uses independence Metropolis-Hastings proposals to facilitate jumps between isolated density components (Andricioaei et al., 2001; Sminchisescu and Welling, 2011). The modes of the target density are often found by a deterministic gradient ascent method started at different initial conditions to discover as many local maxima as possible. A mixture of density components centered at the discovered modes is often used by the independence Metropolis-Hastings (MH) sampler as a proposal distribution. The proposal distribution in this independence MH sampler can be adaptively tuned at regeneration times (Ahn et al., 2013). Darting Monte Carlo methods can be efficient for finding the relative probability masses of the discovered density components, but one of its drawbacks is that an external procedure for finding the modes and approximating the shapes of the modes needs to be employed. Another issue is the unfavorable scaling properties with increasing dimensions, as noted by Ahn et al. (2013).

Wormhole Hamiltonian Monte Carlo (Lan et al., 2014) connects the known locations of the modes by modifying the metric so that the modes are close to each other under the modified metric. The method then runs Riemannian manifold Hamiltonian Monte Carlo, which takes into account the given metric while simulating the Hamiltonian paths (Girolami and Calderhead, 2011).

Tak et al. (2018) developed a novel strategy that attempts a MH move that favors *low* target probability density points before attempting another MH move that favors high density points. In their algorithm, the proposal is first repelled from the the current state and then attracted by a local mode, which may be a different mode than that it started from. The authors, however, could only develop their method for symmetric proposal kernels, such as zero-mean random walk perturbations. Due to the use of random walk kernels, the scaling rate with respect to the space dimension is not likely to be more favorable than methods based on HMC. Moreover, the random walk variance greatly affects the probability of mode hopping, but its tuning may not be straightforward in practice.

## 7 Discussion

We developed a Markov chain Monte Carlo method for sampling from multimodal distributions using tempered Hamiltonian transitions. Since incorrectly sampled posterior distributions can significantly bias inferences, being able to obtain draws from multimodal target distributions can be highly important in many practical situations. Our method enables construction of globally mixing Markov chains when the target distribution is multimodal by facilitating jumps between the isolated modes. It has good scaling properties with increasing space dimensions, since searching of the isolated modes can be carried out efficiently in high dimensions using search paths guided by the gradient of the log target density function.

Our tempered Hamiltonian transitions method can be viewed as a combination of Hamiltonian Monte Carlo and the tempered transitions method. The acceptance probabilities of the proposed candidates can be increased to reasonably high values by scaling the mass of the simulated particle up and down along the simulated paths. This strategy of simulating the Hamiltonian dynamics with varying mass can be alternatively formulated as changing the temperature, as shown in Section 2.3. We developed a tuning strategy that can be used for a wide array of target distributions, by using a certain time scale change in the Hamiltonian equations of motion. We demonstrated that our method can be practically useful by applying it to some mixture distributions and a sensor network localization example. Our method has particular strengths compared to simulated or parallel tempering methods in such cases as when the Gibbs sampler is used for hierarchical models, because time-consuming adaptation of tuning parameters or a burn-in for auxiliary chains is unnecessary when the target distribution changes.

Tempered Hamiltonian transitions (THT) can be used with other MCMC methods for various synergies. Even when the target distribution is not known to be multimodal, the THT kernel can



be employed at regular intervals in order to check if unknown isolated modes exist, while an MCMC kernel that is efficient for unimodal distributions is used for most iteration steps. Such a combined method can increase the reliability of the outputs of the MCMC runs and reduce the risks of biased or incomplete inferences. For highly multimodal target distributions, our method can be used with other approaches such as darting Monte Carlo to improve the overall mixing of the constructed Markov chain. For example, the THT kernel can be interlaced with the independent Metropolis-Hastings kernel in such a way that new modes found by tempered Hamiltonian transitions are recursively added to the mixture distribution used for drawing independent proposals. For target distributions that have widely varying geometric properties at different parts of the space, which often arise in hierarchical Bayesian models, our strategy of scaling the mass may be combined with the position-dependent metric used by Riemannian manifold Hamiltonian Monte Carlo (Betancourt and Girolami, 2015). Detailed development of such combined approach is left as a subject for future study.

**Acknowledgement** The author thanks Yves Atchadé for comments on earlier drafts of this manuscript.

## References

- Ahn, S., Chen, Y. and Welling, M. (2013) Distributed and adaptive darting Monte Carlo through regenerations. In *Artificial Intelligence and Statistics*, 108–116. PMLR.
- Andricioaei, I., Straub, J. E. and Voter, A. F. (2001) Smart darting Monte Carlo. *The Journal of Chemical Physics*, **114**, 6994–7000.
- Atchadé, Y. F. and Liu, J. S. (2010) The Wang-Landau algorithm in general state spaces: applications and convergence analysis. *Statistica Sinica*, 209–233.
- Beskos, A., Pillai, N., Roberts, G., Sanz-Serna, J.-M. and Stuart, A. (2013) Optimal tuning of the hybrid Monte Carlo algorithm. *Bernoulli*, **19**, 1501–1534.
- Betancourt, M. and Girolami, M. (2015) Hamiltonian Monte Carlo for hierarchical models. *Current trends in Bayesian methodology with applications*, **79**, 2–4.
- Bouchard-Côté, A., Vollmer, S. J. and Doucet, A. (2018) The bouncy particle sampler: A nonreversible rejection-free Markov chain Monte Carlo method. *Journal of the American Statistical Association*, **113**, 855–867.
- Brooks, B. R., Brooks III, C. L., Mackerell Jr., A. D., Nilsson, L., Petrella, R. J., Roux, B., Won, Y., Archontis, G., Bartels, C., Boresch, S., Caffisch, A., Caves, L., Cui, Q., Dinner, A. R., Feig, M., Fischer, S., Gao, J., Hodoscek, M., Im, W., Kuczera, K., Lazaridis, T., Ma, J., Ovchinnikov, V., Paci, E., Pastor, R. W., Post, C. B., Pu, J. Z., Schaefer, M., Tidor, B., Venable, R. M., Woodcock, H. L., Wu, X., Yang, W., York, D. M. and Karplus, M. (2009) CHARMM: The biomolecular simulation program. *Journal of Computational Chemistry*, **30**, 1545–1614. URL: <https://onlinelibrary.wiley.com/doi/abs/10.1002/jcc.21287>.
- Darve, E. and Pohorille, A. (2001) Calculating free energies using average force. *The Journal of chemical physics*, **115**, 9169–9183.
- Duane, S., Kennedy, A. D., Pendleton, B. J. and Roweth, D. (1987) Hybrid Monte Carlo. *Physics letters B*, **195**, 216–222.
- Gelman, A., Carlin, J. B., Stern, H. S., Dunson, D. B., Vehtari, A. and Rubin, D. B. (2013) *Bayesian data analysis*. CRC press, 3 edn.

- Gelman, A. and Rubin, D. B. (1992) Inference from iterative simulation using multiple sequences. *Statistical science*, **7**, 457–472.
- Geyer, C. J. (1991) Markov chain monte carlo maximum likelihood. In *Computing science and statistics: Proceedings of 23rd Symposium on the Interface*, 156–163.
- Girolami, M. and Calderhead, B. (2011) Riemann manifold Langevin and Hamiltonian Monte Carlo methods. *Journal of the Royal Statistical Society: Series B (Statistical Methodology)*, **73**, 123–214.
- Gobbo, G. and Leimkuhler, B. J. (2015) Extended Hamiltonian approach to continuous tempering. *Physical Review E*, **91**, 061301.
- Graham, M. and Storkey, A. (2017) Continuously tempered Hamiltonian Monte Carlo. In *Proceedings of the Thirty-Third Conference on Uncertainty in Artificial Intelligence* (eds. G. Elidan, K. Kersting and A. T. Ihler). AUAI Press.
- Hoover, W. G. (1985) Canonical dynamics: Equilibrium phase-space distributions. *Physical review A*, **31**, 1695.
- Ihler, A. T., Fisher, J. W., Moses, R. L. and Willsky, A. S. (2005) Nonparametric belief propagation for self-localization of sensor networks. *IEEE Journal on Selected Areas in Communications*, **23**, 809–819.
- Kou, S., Zhou, Q. and Wong, W. H. (2006) Equi-energy sampler with applications in statistical inference and statistical mechanics. *The Annals of Statistics*, **34**, 1581–1619.
- Lan, S., Streets, J. and Shahbaba, B. (2014) Wormhole Hamiltonian Monte carlo. In *Proceedings of the AAAI Conference on Artificial Intelligence*, vol. 28.
- Landau, D. and Binder, K. (2021) *A guide to Monte Carlo simulations in statistical physics*. Cambridge university press.
- Leimkuhler, B. and Reich, S. (2004) *Simulating Hamiltonian dynamics*, vol. 14. Cambridge university press.
- Lenner, N. and Mathias, G. (2016) Continuous tempering molecular dynamics: A deterministic approach to simulated tempering. *Journal of chemical theory and computation*, **12**, 486–498.
- Liouville, J. (1838) Note on the theory of the variation of arbitrary constants. *Journal de Mathématiques Pures et Appliquées*, **3**, 342–349.
- Luo, R., Wang, J., Yang, Y., Zhu, Z. and Wang, J. (2019) Thermostat-assisted continuously-tempered Hamiltonian Monte Carlo for Bayesian learning. *arXiv preprint arXiv:1711.11511v5*.
- Mangoubi, O., Pillai, N. S. and Smith, A. (2018) Does Hamiltonian Monte Carlo mix faster than a random walk on multimodal densities? *arXiv preprint arXiv:1808.03230*.
- Marinari, E. and Parisi, G. (1992) Simulated tempering: a new Monte Carlo scheme. *EPL (Europhysics Letters)*, **19**, 451.
- Neal, R. M. (1996) Sampling from multimodal distributions using tempered transitions. *Statistics and computing*, **6**, 353–366.
- (2001) Annealed importance sampling. *Statistics and Computing*, **11**, 125–139.

- (2011) MCMC using Hamiltonian dynamics. In *Handbook of Markov chain Monte Carlo* (eds. S. Brooks, A. Gelman, G. Jones and X.-L. Meng), 113–162. CRC press.
  - (2012) *Bayesian learning for neural networks*, vol. 118. Springer Science & Business Media.
- Nosé, S. (1984) A unified formulation of the constant temperature molecular dynamics methods. *The Journal of chemical physics*, **81**, 511–519.
- Park, J. and Atchadé, Y. (2020) Markov chain monte carlo algorithms with sequential proposals. *Statistics and Computing*, **30**, 1325–1345.
- Pompe, E., Holmes, C. and Łatuszyński, K. (2020) A framework for adaptive MCMC targeting multimodal distributions. *The Annals of Statistics*, **48**, 2930–2952.
- Roberts, G. O., Gelman, A. and Gilks, W. R. (1997) Weak convergence and optimal scaling of random walk Metropolis algorithms. *The Annals of Applied Probability*, **7**, 110–120.
- Roberts, G. O. and Rosenthal, J. S. (1998) Optimal scaling of discrete approximations to Langevin diffusions. *Journal of the Royal Statistical Society: Series B (Statistical Methodology)*, **60**, 255–268.
- Sminchisescu, C. and Welling, M. (2011) Generalized darting Monte Carlo. *Pattern Recognition*, **44**, 2738–2748.
- Stan Development Team (2020) RStan: the R interface to Stan. URL: <http://mc-stan.org/>. R package version 2.21.2.
- Swendsen, R. H. and Wang, J.-S. (1986) Replica Monte Carlo simulation of spin-glasses. *Physical review letters*, **57**, 2607–2609.
- Tak, H., Meng, X.-L. and van Dyk, D. A. (2018) A repelling–attracting Metropolis algorithm for multimodality. *Journal of Computational and Graphical Statistics*, **27**, 479–490.
- Vanetti, P., Bouchard-Côté, A., Deligiannidis, G. and Doucet, A. (2017) Piecewise deterministic Markov chain Monte Carlo. *arXiv preprint arXiv:1707.05296*.
- Vehtari, A., Gelman, A., Simpson, D., Carpenter, B. and Bürkner, P.-C. (2019) Rank-normalization, folding, and localization: An improved  $\hat{R}$  for assessing convergence of MCMC. *arXiv preprint arXiv:1903.08008*.
- Wang, F. and Landau, D. P. (2001) Efficient, multiple-range random walk algorithm to calculate the density of states. *Physical review letters*, **86**, 2050–2053.